

CLUSTER-FORMING SITE AFGL 5157: COLLIDING FILAMENTARY CLOUDS AND STAR FORMATION

L. K. DEWANGAN¹

ABSTRACT

We observationally investigate star formation (SF) process occurring in AFGL 5157 (area ~ 13.5 pc \times 13.5 pc) using a multi-wavelength approach. Embedded filaments are seen in the *Herschel* column density map, and one of them is identified as an elongated filamentary feature (FF) (length ~ 8.3 pc; mass $\sim 1170 M_{\odot}$). Five *Herschel* clumps ($M_{clump} \sim 45\text{--}300 M_{\odot}$) are traced in the central part of FF, where an extended temperature structure ($T_d \sim 13.5\text{--}26.5$ K) is observed. In the direction of the central part of FF, the warmer region at $T_d \sim 20\text{--}26.5$ K spatially coincides with a mid-infrared (MIR) shell surrounding a previously known evolved infrared cluster. Diffuse H α emission is traced inside the infrared shell, suggesting the presence of massive stars in the evolved cluster. Based on the surface density analysis of young stellar objects (YSOs), embedded clusters of YSOs are traced toward the central part of FF, and are distributed around the infrared shell. Previously detected H₂O masers, H₂ knots, massive protostar candidates, and H II region are also seen toward the embedded clusters. Using the ¹²CO and ¹³CO line data, the central part of FF is observed at the overlapping zones of two filamentary molecular clouds (length ~ 12.5 pc) around -20 and -17 km s⁻¹, which are also connected in velocity. Our observational results suggest that the formation of massive stars appears to be triggered by a collision of two filamentary molecular clouds, which might have also influenced the birth of YSOs in AFGL 5157.

Subject headings: dust, extinction – H II regions – ISM: clouds – ISM: individual object (AFGL 5157) – stars: formation – stars: pre-main sequence

1. INTRODUCTION

In the era of the space based telescopes like *Spitzer* and *Herschel*, the observational detections of mid-infrared bubbles/shells and filaments have provided several crucial inputs to researchers for understanding the star formation (SF) processes in Galactic star-forming sites (e.g., Churchwell et al. 2006; André et al. 2010, 2014). These observational inputs have been obtained through a detailed analysis of the infrared and sub-millimeter (sub-mm) data. Currently, the study concerning the involvement of filaments in the formation process of dense massive star-forming clumps and young stellar clusters has been received significant attention in the field of SF, which is still debated. In particular, the zones of merging/collision/interaction of filaments are considered a suitable environment for formation of massive OB stars ($\geq 8 M_{\odot}$) and stellar clusters, where one may obtain higher column densities (e.g., Myers 2009; André et al. 2010, 2014; Galván-Madrid et al. 2010; Duarte-Cabral et al. 2011; Schneider et al. 2012; Inoue & Fukui 2013; Nakamura et al. 2012, 2014; Henshaw et al. 2013; Fukui et al. 2014; Dewangan et al. 2017, 2019a,b). In the hydrodynamical simulations of the collision process, massive clumps and cores are produced at the junction of two filamentary molecular clouds or the shock-compressed interface layer (e.g., Habe & Ohta 1992; Anathpindika 2010; Inoue & Fukui 2013; Haworth et al. 2015a,b; Torii et al. 2017; Balfour et al. 2017; Bisbas et al. 2017, and references therein), where massive stars can be formed. However, the observational confirmation of such physical process or a colliding event is a very difficult task, and can be investigated via the knowledge of molecular gas

motion toward the filaments and the zones of interacting/colliding filaments.

Situated at a distance of 1.8 kpc (Snell et al. 1988; Torrelles et al. 1992a), AFGL 5157/IRAS 05345+3157 is an active site of SF, which is also known as NGC 1985 or Mol 11. In the direction of IRAS 05345+3157, an extended shell detected in H₂ was reported, which was found to surround a cluster of infrared sources centered on the IRAS position (Chen et al. 1999, 2003; Reipurth 2008; Varricatt et al. 2010; Wolf-Chase et al. 2017). Chen et al. (1999) suggested the presumptive age of this infrared cluster to be 10⁶ yr, which was referred to as an evolved cluster in AFGL 5157 (see also Chen et al. 2003). These authors suggested that massive stars located in this evolved cluster can be responsible for the H₂ shell through their UV fluorescence. They also reported the H₂ shell as an expanding shell. Using the *Spitzer* 3.6–8.0 μ m images, the infrared emission has been observed toward the H₂ shell (Jiang et al. 2013), which is now referred to as an infrared shell in the present work.

Dust continuum, CS, and NH₃ emissions were observed about 1'.5 away from the evolved cluster or the infrared shell (Verdes-Montenegro et al. 1989; Pastor et al. 1991; Torrelles et al. 1992b; Klein et al. 2005; Lee et al. 2011; Fontani et al. 2012; Jiang et al. 2013). A few H₂O masers and an H II region were reported toward the dense NH₃ core (Torrelles et al. 1992b). Using the VLA 3.6 cm map, Torrelles et al. (1992b) suggested that the H II region is powered by a ZAMS B3 star. Snell et al. (1988) reported a bipolar CO outflow, which was centered on the dense NH₃ core (see also Zhang et al. 2005). On the basis of previously published results in AFGL 5157, a summary figure containing different observed features (i.e., infrared shell, dense core, and H II region) is presented in Figure 1a. Figure 1a shows the *Spitzer* 3.6 μ m image

lokeshd@prl.res.in

¹Physical Research Laboratory, Navrangpura, Ahmedabad - 380 009, India.

(size $\sim 2.7 \text{ pc} \times 2.7 \text{ pc}$) overlaid with the SCUBA 850 μm dust continuum emission contours (Di Francesco et al. 2008; Jiang et al. 2013). Three peaks seen in the 850 μm dust continuum map (i.e., peak1, peak2, and peak3) are also highlighted in the figure, which may trace the dense regions in AFGL 5157 (see also Figure 18 in Reipurth 2008). The infrared shell is also highlighted by the 3.6 μm continuum emission contour. The locations of seven previously observed CS cores (Lee et al. 2011) are also marked in Figure 1a, and are found toward two sub-mm peaks (i.e., peak1 and peak2). Note that the sub-mm peak3 was not covered in the CS observations (see Lee et al. 2011). The direction in the figure is shown in the Galactic coordinates.

Previously, the signatures of ongoing SF were reported through the detection of molecular outflow, H_2O masers, H II region, and several H_2 knots distributed toward the dense NH_3 core (see Figure 6 in Wolf-Chase et al. 2017). All these signposts are seen toward the sub-mm 850 μm continuum peak1 (see Figure 1a). A detailed investigation of the sub-mm 850 μm continuum source (i.e., peak3) is not available in the literature. Recently, using high-resolution NH_3 line observations (resolution $\sim 2'' .5$), Fontani et al. (2012) observed two ammonia filaments in the direction of this dense NH_3 core/region (see Figure 1 in their paper). These authors traced the dense regions with NH_3 (1, 1) emission in a velocity range of $[-17, -18.4] \text{ km s}^{-1}$ (see Table 1 in their paper). They found the seven CS cores, observed by Lee et al. (2011), were within the ammonia filaments. Based on the observed results toward the dense NH_3 core and the H_2 shell, at least two distinct epochs of SF were reported in AFGL 5157 (e.g., Wolf-Chase et al. 2017). The evolved SF phase has been reported toward the infrared cluster or the H_2 shell, while the younger phase of SF (timescale $\sim 10^4\text{--}10^5 \text{ yr}$) is thought to be associated with the dense NH_3 core (see also Figure 3 in Chen et al. 2003). It was also argued that the evolved infrared cluster might have triggered the younger phase of SF associated with the dense NH_3 core and northwest areas (Chen et al. 2003). Note that all the earlier works were mainly focused to an area of $\sim 1.8 \text{ pc} \times \sim 1.8 \text{ pc}$ containing AFGL 5157.

The study of the physical environment at large-scale ($> 10 \text{ pc}$) is not yet reported in AFGL 5157. We do not find any study for examining embedded filaments, young stellar objects (YSOs), and the velocity structure of molecular gas on a wide-scale around AFGL 5157. Our present paper focuses on understanding the exact SF mechanisms occurring in AFGL 5157. In this context, a multi-wavelength approach has been adopted in this paper. A detailed analysis of $^{12}\text{CO}(1-0)$ and $^{13}\text{CO}(1-0)$ gas has been performed comparing its distribution against the infrared and sub-mm images. To trace the signatures of SF activity, a careful analysis of embedded YSOs is carried out for a large-scale area containing AFGL 5157.

In Section 2, we present details of the adopted data sets. Section 3 provides the information of the physical environment at large-scale in AFGL 5157. Section 4 deals with the possible SF processes operational in our selected target site. Finally, Section 5 gives the main conclusions of this paper.

2. DATA

Our present work deals with an area of $\sim 0^\circ.43$ (13.5 pc) $\times 0^\circ.43$ (13.5 pc) (central coordinates: $l = 176^\circ.445$; $b = 0^\circ.215$) containing AFGL 5157. We analyzed the data sets in the optical, infrared, sub-mm, and radio regimes, which were obtained from several surveys. Table 1 lists all these surveys.

Five College Radio Astronomy Observatory (FCRAO) $^{12}\text{CO}(1-0)$ and $^{13}\text{CO}(1-0)$ line data (velocity resolution $\sim 0.25 \text{ km s}^{-1}$) were employed in this paper, which were observed as part of the E-OGS. The E-OGS is known as an extended coverage of the FCRAO Outer Galaxy Survey (OGS; Heyer et al. 1998). Typical rms values for the spectra are 0.25 K for ^{12}CO and 0.2 K for ^{13}CO (e.g., Heyer et al. 1996). The CO data cubes were given by M. Heyer and C. Brunt (through private communication). The data cubes of ^{12}CO and ^{13}CO were smoothed using a Gaussian function with a full-width at half-maximum of 3 pixels to improve sensitivity.

We also downloaded the *Spitzer* post-Basic Calibrated Data (PBCD) images at 3.6, 5.8, and 8.0 μm from the *Spitzer* Heritage Archive (ID: 50244; PI: G. Fazio). These images (plate scale $\sim 0''.6/\text{pixel}$) were available only for an area of $\sim 5'.5 \times \sim 5'.5$ hosting AFGL 5157.

3. ANALYSIS AND RESULTS

3.1. Multi-band picture of AFGL 5157

In order to probe the physical environment of AFGL 5157, multi-wavelength continuum images are carefully examined, which span from optical $\text{H}\alpha$, infrared to radio wavelengths.

3.1.1. Multi-wavelength continuum images

As highlighted in Section 1, in the direction of AFGL 5157, Figure 1a summarizes previously reported features (i.e., infrared shell, dense core, and H II region) within an area of $\sim 1.8 \text{ pc} \times \sim 1.8 \text{ pc}$. A large-scale view of AFGL 5157 (size $\sim 13.5 \text{ pc} \times 13.5 \text{ pc}$) at 250 μm is shown in Figure 1b. This sub-mm image shows the existence of embedded filaments. We highlight representative filaments using arrows in Figure 1b. The embedded filaments appear to be directed towards the location of AFGL 5157 and the emission peaks (i.e., H II region and dense core) in and around the region. In Figure 1b, the position of the previously detected H II region (from Torrelles et al. 1992b) is marked by a star, which is embedded in the dense NH_3 core reported by Torrelles et al. (1992b). The quantitative information of these filaments is presented in Section 3.1.2.

Using the *Spitzer* 8.0 μm image (resolution $\sim 2''$), Figure 1c shows a zoomed-in view of the area containing AFGL 5157. In Figure 1c, the location of the infrared shell is also indicated by the emission contour at 8.0 μm (see also Figure 1a). Furthermore, the absorption features against the Galactic background in the 8.0 μm image are seen in the Galactic northeast to southwest directions around the infrared shell. It enables us to identify the infrared dark clouds (IRDCs) in AFGL 5157 (see arrows in Figure 1c). In addition to the IRDCs and the infrared shell, the *Spitzer* 8.0 μm image also reveals noticeable diffuse emission, which is highlighted by arrows in Figure 1c. In Figure 1d, the sub-mm image at 160 μm (resolution $\sim 12''$) traces the bright emission toward the IRDCs, and the infrared shell (see arrows in Figure 1d).

One can also note that the sub-mm 850 μm continuum peaks (i.e., peak1, peak2, and peak3) are also found toward the IRDCs (see Figures 1a and 1c).

Figure 1e displays the inverted gray-scale IPHAS H α image. The locations of the infrared shell, the H II region, and IRAS 05345+3157 are also indicated in Figure 1e. The diffuse H α emission is known as a tracer of the ionized emission, which is distributed within the infrared shell powered by massive stars located in the evolved infrared cluster (e.g., Chen et al. 2003). In Figure 1f, we display the *Spitzer* ratio map of 4.5 μm /3.6 μm emission, indicating the presence of bright and black regions. More information on the procedures for obtaining the *Spitzer* ratio map can be found in Dewangan et al. (2017). The positions of previously reported Molecular Hydrogen emission-line Objects (MHOs; from Wolf-Chase et al. 2017) are also shown in the figure (see hexagons in Figure 1f). In the ratio map, the bright regions show the excess of 4.5 μm emission, and are not associated with the diffuse H α emission. On the other hand, the domination of 3.6 μm emission is inferred through the black or dark gray regions seen in the ratio map. One can note that polycyclic aromatic hydrocarbon (PAH) emission at 3.3 μm is included in the IRAC 3.6 μm band, and a prominent molecular hydrogen line emission ($\nu = 0-0 S(9)$; 4.693 μm) is covered in the IRAC 4.5 μm band. Hence, the regions with the excess of 4.5 μm emission (i.e., bright regions) appear to trace the outflow activities in AFGL 5157, which are distributed toward the IRDCs. This argument is supported by the fact that the bright regions in the ratio map are spatially matched with the positions of MHOs (see Figure 1f), which are driven by YSOs (e.g., Chen et al. 2003; Wolf-Chase et al. 2017). We also find that the bright regions in the ratio map and the positions of MHOs are found mainly toward the IRDCs or the sub-mm 850 μm continuum peaks, depicting the locations of ongoing SF in AFGL 5157. Taking into account the inclusion of 3.3 μm PAH feature in the 3.6 μm band, the boundaries of the shell-like feature hosting the diffuse H α emission seem to trace photodissociation regions (or photon-dominated regions, or PDRs). In the Galactic northern direction, the observed diffuse 8.0 μm emission also hints the presence of an extended PDRs in the selected site. It is based on the fact that the *Spitzer* band at 8.0 μm contains PAH features at 7.7 and 8.6 μm .

3.1.2. *Herschel* filaments in AFGL 5157

In order to further explore the IRDCs, filaments, and infrared shell, we present the *Herschel* temperature and column density ($N(\text{H}_2)$) maps (resolution $\sim 12''$) in Figures 2a and 2b, respectively. We retrieved the final processed *Herschel* temperature and column density ($N(\text{H}_2)$) maps (resolution $\sim 12''$) from the publicly available site¹. These maps were produced as a part of the EU-funded ViaLactea project (Molinari et al. 2010b). To produce these *Herschel* maps, the Bayesian *PPMAP* procedure (Marsh et al. 2015) was employed to the *Herschel* continuum data by Marsh et al. (2017).

At least three filaments are highlighted in both the *Herschel* maps (see vertical lines in Figures 2a and 2b). Among these filaments, an elongated filamentary feature

(length ~ 8.3 pc) is identified using a column density contour with a level of $3.94 \times 10^{21} \text{ cm}^{-2}$, which is marked in Figures 2a and 2b. The total mass of the filamentary feature is estimated to be $\sim 1170 M_\odot$, and is computed using the equation, $M_{\text{area}} = \mu_{\text{H}_2} m_{\text{H}} \text{Area}_{\text{pix}} \Sigma N(\text{H}_2)$, where μ_{H_2} is the mean molecular weight per hydrogen molecule (i.e., 2.8), Area_{pix} is the area subtended by one pixel (i.e., $6''/\text{pixel}$), and $\Sigma N(\text{H}_2)$ is the total column density (see also Dewangan et al. 2017). The other two filaments show a temperature range of about 13–13.5 K, and seem to be directed toward the central part of the filamentary feature. The locations of the infrared shell and the IRDCs are located within the central part of the filamentary feature, which is indicated in the *Herschel* maps. One can note that a column density deficient region is found in the direction of the infrared shell (see Figure 2b and also Figure 3a). The central part of the filamentary feature is traced using a column density contour with the level of $\sim 9-11 \times 10^{21} \text{ cm}^{-2}$, where the maximum value of the column density is estimated to be $\sim 3.7 \times 10^{23} \text{ cm}^{-2}$. Earlier, Krumholz & McKee (2008) reported a threshold value of 1 gm cm^{-2} (or corresponding column density $\sim 3 \times 10^{23} \text{ cm}^{-2}$) for formation of massive stars. Hence, it is likely that massive stars can be formed within the central part of the filamentary feature. Interestingly, Lee et al. (2011) suggested the presence of massive protostar candidates toward the dense cores. The *Herschel* temperature map shows an extended temperature structure toward the central part of the filamentary feature. The infrared shell is spatially located inside this temperature structure, and is traced in a temperature range of about 20–26.5 K. Furthermore, a cold region ($T_d \sim 13.5-15$ K) inside the temperature structure is also found in the *Herschel* temperature map. As mentioned earlier, the signatures of outflow activities are mainly found toward the IRDCs, where higher column density materials are observed in the *Herschel* column density map. Using the column density map and the *clumpfind* algorithm (Williams et al. 1994), we have identified twenty three clumps in our selected target site, and have also computed their physical parameters (i.e., mass (M_{clump}), radius (R_{clump}), and average volume density (n_{H_2})). To find the clumps, we provided several column density contour levels (i.e., $(3.9, 5.0, 6.0, 7.0) \times 10^{21} \text{ cm}^{-2}$) as an input parameter for the *clumpfind*, where the lowest contour level was chosen at about 6σ . In Figure 2c, the boundaries of these clumps are shown along with their labels. The values of M_{clump} , R_{clump} , and n_{H_2} of each *Herschel* clump are listed in Table 2. Here, the average volume density ($n_{\text{H}_2} = 3M_{\text{clump}}/(4\pi R_{\text{clump}}^3 \mu_{\text{H}_2} m_{\text{H}})$) of each clump is estimated using the values of M_{clump} and R_{clump} . The calculations assume that each clump has a spherical geometry. The values of n_{H_2} for all the clumps are found between 2200 and 5500 cm^{-3} . In the direction of the elongated filamentary feature, several clumps are found (see IDs 8–22 in Figure 2c and also Table 2). Among these clumps, seven clumps (e.g., 13, 15, 16, 17, 19, 21, and 22) have masses more or equal to $30 M_\odot$, which are also small scale clumps except the clump ID 16. The clump ID 16 is located toward the central part of the filamentary feature (see also Figure 3a). Additionally, the sub-mm emission toward the clump 13 is prominently seen in the *Herschel* images.

¹ <http://www.astro.cardiff.ac.uk/research/ViaLactea/>

Using the *Herschel* column density contour map, a zoomed-in view of the central part of the filamentary feature is presented in Figure 3a. As pointed out above, the *Herschel* column density map shows no emission toward the region, where the diffuse H α emission (or infrared shell) is observed. However, in the direction of clump ID 16, we do not find any column density deficient region due to the choice of a lower column density threshold in the *clumpfind*. Hence, in Figure 3a, we have further employed the *clumpfind* using higher column density contour levels (i.e., (9, 11, 13, 15, 19, 23, 30, 40, 50, 60) $\times 10^{21}$ cm $^{-2}$). A total of five clumps are identified toward the central part of the filamentary feature (or the clump ID 16), and are labeled as A, B, C, D, and E in the figure. The positions of these clumps are marked in Figure 3b, and their boundaries are also indicated in the figure. In Figure 3b, one can also clearly see the column density deficient region toward the diffuse H α emission (or infrared shell). Table 2 also lists the values of M_{clump} , R_{clump} , and n_{H_2} of these five clumps. The clump masses vary between 45 M_{\odot} and 300 M_{\odot} . The values of n_{H_2} are obtained between $\sim 1.3 \times 10^4$ and $\sim 5.5 \times 10^4$ cm $^{-3}$. These dense and massive clumps (i.e., “A”–“E”) are distributed toward the IRDCs.

Using the *Herschel* temperature map, a zoomed-in view of the central part of the filamentary feature is also shown in Figure 3c. The cold region ($T_d \sim 13.5$ –15 K) is associated with the massive clump “A”, and is surrounded by a relatively warm dust emission ($T_d \sim 15$ –18 K). In the literature, we find that the clump “A” has been explored extensively, and is associated with the previously known signatures of ongoing (massive) SF (see also the sub-mm 850 μ m continuum peak1 in Figure 1c). In the direction of the infrared shell, the *Herschel* column density and temperature maps show the low column density tracing the cleared out region associated with the warm dust emission ($T_d \sim 20$ –26.5 K) or the evolved infrared cluster. Using the WISE 12 μ m image, Figure 3d shows a zoomed-in view of the central part, where the positions of the identified seven CS cores (from Lee et al. 2011) are also marked. All the CS cores are depicted toward the cold region ($T_d \sim 13.5$ –15 K) traced in the *Herschel* temperature map. The relatively warmer region ($T_d \sim 15$ –18 K) is seen in the direction of the area, where the noticeable diffuse 8.0 and 12.0 μ m emission is evident (see arrows in Figure 1c). It seems that the observed extended temperature structure indicates the distribution of the warm dust emission in the PDRs (see Figure 3c). It implies that the physical environment of AFGL 5157 appears to be affected by the intense energetic feedback of massive stars (i.e., stellar wind, ionized emission, and radiation pressure).

3.2. Selection and distribution of embedded population in AFGL 5157

Infrared photometric data have been used to study the embedded YSOs in AFGL 5157. Using the 2MASS, UKIDSS-GPS, and GLIMPSE360 photometric catalogs, we have utilized the dereddened color-color space ($[K-[3.6]]_0$ and $[[3.6]-[4.5]]_0$) and the color-magnitude space (H–K/K) to identify the YSOs. The photometric magnitudes (at 3.6 and 4.5 μ m) were obtained from the Glimpse360 highly reliable catalog. We selected only

those sources that have photometric magnitude error of 0.2 and less in the 3.6 and 4.5 μ m bands. We also utilized the photometric HK data from the UKIDSS GPS tenth archival data release (UKIDSSDR10plus) catalog and the 2MASS. Using the conditions given in Lucas et al. (2008) and Dewangan et al. (2015), only reliable UKIDSS GPS photometric data were downloaded in this work. 2MASS H and K photometric data were also obtained for bright sources that were saturated in the GPS catalog. We considered only those 2MASS sources that have photometric magnitude error of 0.1 and less in each band.

Figure 4a displays the dereddened color-color plot ($[K-[3.6]]_0$ and $[[3.6]-[4.5]]_0$) of point-like sources. The dereddened colors were computed using the photometric magnitudes of sources at 1–5 μ m and the color excess ratios listed in Flaherty et al. (2007). Following the several conditions suggested in Gutermuth et al. (2009) (see also Dewangan et al. 2017), Class I and Class II YSOs are identified in our selected site. This color-color space gives 71 (9 Class I and 62 Class II) YSOs (see circles and triangles in Figure 4a). Figure 4b shows the color-magnitude plot (H–K/K) of point-like sources. We find the infrared-excess sources with H–K > 1 mag. This color condition is found via the color-magnitude analysis of a nearby control field. The color-magnitude space gives 74 additional YSO candidates, which are not common with the YSOs identified using the dereddened color-color space. These two schemes yield a total of 145 YSOs in the selected site, and their positions are marked in the *Herschel* column density map (see Figure 4c). A majority of these YSOs are distributed toward the central part of the filamentary feature observed in the *Herschel* column density map, where five dense clumps A, B, C, D, and E are investigated (see Figures 3b and 4c). Furthermore, YSOs are also found toward other *Herschel* clumps (e.g., 13, 15, 17, 18, 19, and 21; see Figures 2c and 4c). Overlay of these selected YSOs on the *Spitzer* 8.0 μ m image is shown in Figure 5a.

As previously mentioned that the coverage of *Spitzer* 8.0 μ m image (plate scale $\sim 0''.6$ /pixel) is available for an area of $\sim 5'.5 \times \sim 5'.5$ hosting AFGL 5157. Hence, in order to select additional YSOs in this selected area, we have employed the *Spitzer* color-color plot ($[3.6]-[4.5]$ vs. $[5.8]-[8.0]$), which is presented in Figure 5b. This color-color space is useful for identifying the deeply embedded protostars (e.g., Gutermuth et al. 2009). We extracted photometry of sources at 5.8 and 8.0 μ m, and the counterparts of these sources were obtained from the Glimpse360 photometric catalogs at 3.6 and 4.5 μ m. Aperture photometry was performed on the *Spitzer* images (at 5.8 and 8.0 μ m) with a $2''.4$ aperture and a sky annulus from $2''.4$ to $7''.3$ using IRAF. The zero points for these apertures (including aperture corrections) are 17.4899 and 16.6997 mag for the 5.8 and 8.0 μ m bands, respectively (see also Dewangan et al. 2012, for further information on the *Spitzer* photometry). Following the various conditions given in Gutermuth et al. (2009) (see also Dewangan et al. 2012), additional YSOs are identified. We have classified these selected YSOs into different evolutionary stages based on their slopes of the spectral energy distribution ($\alpha_{3.6-8.0}$) computed from 3.6 to 8.0 μ m (i.e., Class I ($\alpha_{3.6-8.0} > -0.3$), Class II ($-0.3 > \alpha_{3.6-8.0} > -1.6$), and Class III ($-1.6 > \alpha_{3.6-8.0} > -2.56$)) (e.g., Lada et al. 2006). We select

additional 22 YSOs (14 Class I and 8 Class II) using this scheme, which are plotted in Figure 5c. These selected YSOs are not overlapped with that YSOs shown in Figure 5a. Photometric information of all the selected YSOs is given in Table 3. Figure 5d shows the overlay of the selected YSOs on the *Spitzer* ratio map of $4.5\ \mu\text{m}/3.6\ \mu\text{m}$ emission, revealing the association of YSOs with the bright regions due to an excess of $4.5\ \mu\text{m}$ emission (or outflow activities; see Section 3.1).

Figure 6a displays a surface density contour map of 135 YSOs distributed in the area shown in Figure 5c. The surface density contours of YSOs are shown with the levels of 5, 10, 15, 20, 30, 40, 60, and 85 YSOs/pc², suggesting the intense ongoing SF activities in the selected site. In Figure 6a, the *Herschel* column density contours (in red), the infrared shell (in cyan), and the diffuse H α emission contour (in blue) are also highlighted in the surface density contour map. We employed the nearest-neighbour (NN) method to estimate the surface density contours of the selected YSOs (see Casertano & Hut 1985; Gutermuth et al. 2009; Bressert et al. 2010; Dewangan et al. 2017, for more details). Adopting the similar analysis as carried out in Dewangan et al. (2017), the surface density map of all the selected YSOs has been produced using a $5''$ grid and 6 NN at a distance of 1.8 kpc. The surface density contours with the levels of 30, 40, 60, and 85 YSOs/pc² are shown in Figures 6b, 6c, and 6d. In Figure 6b, we have also marked the positions of the identified seven CS cores (from Lee et al. 2011). Using the continuum map at 2.7 mm and the CS line data, Lee et al. (2011) also reported that massive protostar candidates are forming in two of these dense cores. In Figures 6c and 6d, the surface density contours are overlaid on the *Herschel* column density and temperature maps, respectively. Figure 6d reveals a spatial correlation between the embedded clusters (with surface density ≥ 30 YSOs/pc²) and the higher column density materials (including *Herschel* clumps and dense CS cores).

Together, the central part of the filamentary feature is associated with massive dust clumps, dense CS cores, massive protostar candidates, and clusters of YSOs.

3.3. Kinematics of molecular gas

To study the molecular gas associated with AFGL 5157, Figures 7a and 7b show the ¹²CO(J = 1–0) and ¹³CO(J = 1–0) intensity maps (moment-0) integrated over a velocity range of -22 to $-15\ \text{km s}^{-1}$, respectively. The locations of the filamentary feature, infrared shell, and previously known H II region are highlighted in both the molecular maps. We find that all the *Herschel* filaments are embedded in the molecular cloud associated with AFGL 5157. Note that our molecular line data, having coarse resolutions, do not allow to trace the gas motions along/into the filamentary structures seen in the *Herschel* data. However, these molecular line data enable us to study the large-scale molecular cloud motions. The observed ¹²CO and ¹³CO profiles are presented in Figure 7c. The spectra are produced by averaging the area highlighted by a solid circle in Figure 7b, which is located toward the central part of the filamentary feature. The ¹²CO profile reveals two velocity peaks (around -20 and $-17\ \text{km s}^{-1}$), while a broad profile of ¹³CO is observed toward our selected area (see a

solid circle in Figure 7b). Figure 8 displays the average ¹²CO and ¹³CO spectra in the direction of twelve small regions (i.e., p1 to p12; see corresponding boxes in Figure 7a). The selected region “p3” covering larger area and the small circle in Figure 7b are very close, where one may expect similar molecular profiles. In the ¹²CO spectrum, two peaks (around -20 and $-17\ \text{km s}^{-1}$) are clearly seen in the direction of the region p3, while the peak of the corresponding ¹³CO spectrum (around $-18.5\ \text{km s}^{-1}$) is found toward a dip between two peaks seen in the ¹²CO spectrum (see also Figure 7c). In the direction of other small regions (or away from the central part of the filamentary feature), the peak in the ¹²CO spectrum nearly matches with the peak in the ¹³CO profile. Hence, in the direction of the region p3, the shift of velocity in the ¹²CO and ¹³CO could be due to the presence of self-absorption of ¹²CO line around $-18.5\ \text{km s}^{-1}$. It can be treated as an example of a blue-asymmetric self-absorption profile. Based on a relatively low ratio value (< 2.5) of ¹²CO/¹³CO at $-18.5\ \text{km s}^{-1}$, the ¹²CO self-absorption feature is found toward the elongated filamentary feature (see a summary figure in this Section and also Section 4 for more details). If we use the ratio value less than one (i.e., < 1.0) then one may notice significant self-absorption in the direction of the *Herschel* clump “D”, which is an area between the *Herschel* clump “E” (or the sub-mm peak3) and the infrared shell.

Figures 9 and 10 display the integrated ¹²CO and ¹³CO velocity channel maps from -23 to $-14\ \text{km s}^{-1}$, respectively. Each velocity channel map is produced by integrating the emission over $1\ \text{km s}^{-1}$ velocity interval. The location of the filamentary feature is also marked in both the channel maps. The velocity channel maps also suggest the presence of two velocity components (see panels at $[-17, -16]$ and $[-20, -19]\ \text{km s}^{-1}$ in Figures 9 and 10). Figures 11a and 11b present the first moment maps of ¹²CO and ¹³CO, respectively. The moment map is known to depict the intensity-weighted mean velocity of the emitting gas. Figure 11c displays a color-composite image of AFGL 5157 with the ¹³CO maps at $[-17, -16]$ and $[-20, -19]\ \text{km s}^{-1}$ in red and green, respectively. The filamentary feature observed in the *Herschel* column density map is also highlighted in Figures 11a, 11b, and 11c. It seems that this color-composite image reproduces the velocity field as observed in the first moment maps of ¹²CO and ¹³CO. Therefore, it implies the presence of two elongated filamentary molecular clouds in the direction of our selected target area (see Figure 11b). In Figure 11d, we have overlaid the ¹³CO emission contours at $[-17, -16]$ and $[-20, -19]\ \text{km s}^{-1}$ on the *Herschel* column density map, suggesting the distribution of the molecular gas associated with two cloud components (around -20 and $-17\ \text{km s}^{-1}$) toward the column density materials. Interestingly, the central part of the filamentary feature is found at the common zones of the clouds at $[-17, -16]$ and $[-20, -19]\ \text{km s}^{-1}$, illustrating the spatial connections of the two cloud components. Previously, the NH₃ (1, 1) emission toward the dense cores was observed around $-17\ \text{km s}^{-1}$ (see Table 1 in Fontani et al. 2012). Furthermore, in Figure 7c, we have also observed an almost flattened profile between two velocity peaks around -20 and $-17\ \text{km s}^{-1}$, sug-

gesting the velocity connections of these two cloud components. Figure 12a shows the integrated ^{12}CO emission map, which is displayed only for the comparison (see also Figure 7a). Figures 12b and 12c display the Latitude-velocity map of ^{12}CO and Longitude-velocity map of ^{12}CO , respectively. Both these position-velocity maps reveal two velocity components (around -20 and -17 km s^{-1}). In the velocity space, these two velocity peaks are also interconnected by a lower-intensity intermediate velocity emission, suggesting their connection in velocity. In Figures 13a and 13b, we have also obtained the position-velocity maps of ^{12}CO and ^{13}CO along the axis (i.e., X1–X2) as marked in Figure 12a, respectively. Both these position-velocity maps also favour the presence of two velocity components, and their connection in velocity. In the direction of the central part of the filamentary feature, Figure 14a displays the spatial connections of two cloud components of ^{13}CO (at $[-17, -16]$ and $[-20, -19] \text{ km s}^{-1}$) against the surface density map of YSOs.

In the large-scale area, a schematic figure is shown in Figure 14b, which displays the spatial distribution of two clouds (around -20 and -17 km s^{-1}) and the area associated with the intense SF activities (see a broken circle in Figure 14b). We have also highlighted the locations of the embedded clusters by two arc-like curves in the figure. The location of the ^{12}CO self-absorption feature is also indicated by solid magenta contours in the figure.

An implication of these results is discussed in Section 4.

4. DISCUSSION

In this paper, we have employed the *Herschel* column density and temperature maps, which have provided a new pictorial view of AFGL 5157 (see Figure 2). These maps have revealed at least three embedded filaments in the selected target field (see Section 3.1). Among these filaments, one elongated filamentary feature (having length $\sim 8.3 \text{ pc}$ and mass $\sim 1170 M_{\odot}$) is depicted, and its central part is visually seen as the junction point of the other filaments (see Figure 2b). Embedded clusters of YSOs are depicted toward the central part, and are distributed around the infrared shell. Our observational results reveal that SF activities are concentrated mainly toward the central part of the filamentary feature (see Section 3.2). The warmest region (at $T_d \sim 20\text{--}26.5 \text{ K}$) in the central part of the filamentary feature spatially matches with the infrared shell, which hosts the diffuse $\text{H}\alpha$ emission as well as the previously known evolved infrared cluster. The *Herschel* column density map displays no emission toward the warmest region or the area with the diffuse $\text{H}\alpha$ emission, suggesting the impact of the massive stars in their vicinity. Different pressure components driven by massive stars (i.e., pressure of an HII region (P_{HII}), radiation pressure (P_{rad}), and stellar wind ram pressure (P_{wind})) can be attributed to the feedback of massive stars (e.g., Bressert et al. 2012; Dewangan et al. 2017). In Section 3.1, the presence of the PDRs in the central part of the filamentary feature is inferred, and the extension of the PDRs is depicted through the detection of the extended temperature structure in the *Herschel* temperature map. These results together indicate that the physical environment of AFGL 5157 appears to be influenced by massive stars located in the evolved infrared cluster (age $\sim 10^6\text{--}10^7 \text{ yr}$; Chen et al.

2003). Mean ages of Class I and Class II YSOs have been reported to be $\sim 0.44 \text{ Myr}$ and $\sim 1\text{--}2 \text{ Myr}$, respectively (Evans et al. 2009). Hence, it is likely that the expanding shell associated with the evolved infrared cluster might have influenced the birth of the youngest population in the site (see also Chen et al. 2003). However, the birth process of massive stars and the infrared cluster is not yet understood in AFGL 5157.

In Section 3.3, we find that the observed velocity field in the first moment maps of ^{12}CO and ^{13}CO can be explained by the presence of two filamentary molecular clouds (length $\sim 12.5 \text{ pc}$) around -20 and -17 km s^{-1} in the direction of our selected target area. Therefore, the hypothesis that the star formation activity associated with AFGL 5157 involves a cloud-cloud collision should be explored. To examine SF triggered by head-on collisions, Balfour et al. (2017) carried out the smoothed particle hydrodynamics simulations and found the filamentary structures within colliding clouds. Previously, there are some limited examples available in the literature (such as, W33A (Galván-Madrid et al. 2010), L1641-N (Nakamura et al. 2012), Rosette Nebula (Schneider et al. 2012), Infrared dark cloud G035.39–00.33 (Henshaw et al. 2013), Serpens (Duarte-Cabral et al. 2011; Nakamura et al. 2014), Sh 2-237 (Dewangan et al. 2017), and AFGL 5142 (Dewangan et al. 2019b)), where the collision/interaction of filaments has been proposed to explain the SF history. As mentioned in Section 1, theoretically, massive stars and clusters of YSOs can be produced by the collision/interaction of two clouds (e.g., Loren 1976; Habe & Ohta 1992; Inoue & Fukui 2013; Fukui et al. 2014, and references therein). Habe & Ohta (1992) studied theoretical simulations of head-on collisions of two non-identical clouds, and found gravitationally unstable cores/clumps at the interface of these two clouds due to the effect of their compression. Hence, the shock-compressed interface layer can be heated, while the molecular clouds on the trailing side will be cold (e.g., Loren 1976). In this context, one may observe self-absorption of ^{12}CO line toward the interface of cloud-cloud collisions (Loren 1976). In the simulation of Habe & Ohta (1992), a small cloud creates a cavity in the large cloud in the collision event. After the formation of massive OB stars, the cavity is filled with the ionized emission. Additionally, in the collision process, one can find the spatial and velocity connections of two molecular clouds (e.g., Torii et al. 2017; Dewangan et al. 2019a). One can also expect an almost flattened profile between two velocity peaks in the molecular spectrum. Furthermore, in the velocity space, one can also observe a connection of two molecular clouds through a feature at the intermediate velocity range, suggesting the presence of a bridge-like feature. The observed bridge feature may indicate the existence of a compressed layer of gas due to two colliding clouds/flows (e.g., Haworth et al. 2015a,b; Torii et al. 2017).

Based on the analysis of the ^{12}CO and ^{13}CO line data, a significant self-absorption of ^{12}CO line at -18.5 km s^{-1} is evident toward the common areas of two clouds (see Figure 14b and also Section 3.3). The peak contours of the self-absorption feature are seen away from the peaks of the two cloud components (i.e., -20 and -17 km s^{-1}). We also find that the peak of the ^{12}CO

emission around -17 km s^{-1} is seen toward the *Herschel* clump “A”, while the peak of the ^{12}CO emission around -20 km s^{-1} is nearly seen in the direction of the *Herschel* clump “E”. Double peaks in the CS spectra toward two dense cores have also been observed by Lee et al. (2011), which are seen toward the embedded clusters (see Section 3.2). In the velocity space of ^{12}CO , a bridge-like feature at the intermediate velocity range between two velocity peaks (i.e., -20 and -17 km s^{-1}) is noticed (see Figures 12b and 12c), which may be due to self-absorption (see Section 3.3). However, the weaker emission connecting two velocity components is also seen in the position-velocity map of ^{13}CO (see Figure 13b). Hence, there is also a signature of a bridge-like feature in ^{13}CO , indicating the existence of the turbulent gas excited by the collision process. High resolution optically thin line data will be useful to further examine the bridge-like feature. Previously, using the ^{12}CO spectra, Torii et al. (2017) also reported a similar feature in the star-forming region M20 (see their Figure 14), which is believed to be a site of cloud-cloud collision.

The spatial fit of “Keyhole/intensity-depression” and “Key/intensity-enhancement” features is considered as an another piece of observational evidence of the collision event (e.g., Torii et al. 2017; Fukui et al. 2018; Dewan-gan et al. 2019a). In general, an intensity/gas deficient region in the molecular map is referred to as a “Key-hole/cavity” feature, while an intensity-enhancement area is called as a “Key” feature (see Fukui et al. 2018, for more details). Using the *Herschel* column density map (resolution $\sim 12''$), a low column density area or intensity-depression or cavity is seen around the *Herschel* clumps “A”–“D”, and is filled with the diffuse H α emission/ionized gas (see Figure 3a). However, due to coarse beam sizes ($\sim 45''$) of the molecular line data, our molecular maps do not permit to explore the “Keyhole” and “Key” features toward the central part of the *Herschel* filamentary feature.

In AFGL 5157, the central part of the *Herschel* filamentary feature is observed at the overlapping zones of the two filamentary molecular clouds, where embedded clusters of YSOs, evolved infrared clusters, massive protostar candidates, massive stars, and massive clumps are located (see Figures 14a and 14b). In the direction of the central part, a very high value of the column density is found to be $\sim 3.7 \times 10^{23} \text{ cm}^{-2}$. Overall, the observed SF activities in AFGL 5157 are mainly depicted toward the common areas of the filamentary molecular clouds. Keeping in mind the predictions of the collision process, our observational findings suggest that the collision scenario is applicable in AFGL 5157. In this context, large-scale and high resolution optically thin molecular line observations will be helpful to further confirm the collision hypothesis in AFGL 5157.

In order to compute the collision time-scale, we have followed the works of Henshaw et al. (2013) and Dewan-gan et al. (2019b). Using the equation 1 given in Dewan-gan et al. (2019b), the time-scale of the accumulation of material at the collision points or the collision time-scale can be calculated with the knowledge of the collision length-scale, the observed relative velocity, and the ratio of the mean densities of the pre- and post-collision regions. It is noted that the observational determination of

the exact ratio of the mean densities of the pre- and post-collision regions is not possible using the data utilized in this paper, and is beyond the scope of the present work. However, the increase of density in the post-collision region is expected in the collision process. Therefore, the density ratio is likely to be higher than unity. We have computed the collision length-scale and the observed relative velocity to be $\sim 3.95 \text{ pc}$ ($= 2.8 \text{ pc}/\sin(45^\circ)$) and $\sim 4.25 \text{ km s}^{-1}$ ($= 3.0 \text{ km s}^{-1}/\cos(45^\circ)$), respectively. A viewing angle of the collision is adopted to be 45° in this calculation. Taking into account a range of the ratios of densities (i.e., 1–10), the typical collision timescales are computed to be ~ 1.8 – 18.6 Myr , indicating that the collision/interaction happened earlier than 1.8 Myr in AFGL 5157. Even though, there is uncertainty in the calculation, but the collision timescale can be referred to as indicative value. Considering the stellar ages discussed in this section and the collision timescale, it is possible that the collision/interaction of the two filamentary clouds might have triggered the birth of massive stars and YSOs in AFGL 5157.

5. SUMMARY AND CONCLUSIONS

The present paper is directed at gaining an understanding of the formation process of massive stars and young stellar clusters in AFGL 5157. We have investigated an area (size ~ 0.43 (13.5 pc) \times 0.43 (13.5 pc)) of AFGL 5157. In this paper, the *Herschel* sub-mm continuum images and molecular line data are carefully examined to probe the physical environment of the selected site, and have allowed us to shed light on the ongoing physical process. The distribution of the embedded YSOs is studied using the photometric data at 1 – $8 \mu\text{m}$. The observational findings of the present work are as follows:

- In the selected site, at least three embedded filaments are visually seen in the *Herschel* column density and temperature maps. Among these filaments, an elongated filamentary feature (having length $\sim 8.3 \text{ pc}$ and mass $\sim 1170 M_\odot$) is identified with the $N(\text{H}_2)$ contour at $3.94 \times 10^{21} \text{ cm}^{-2}$.
- The central part of the filamentary feature is traced using the $N(\text{H}_2)$ contour at ~ 9 – $11 \times 10^{21} \text{ cm}^{-2}$, and contains the previously detected H_2O masers, H_2 knots, massive protostar candidates, and H II region.
- The other two filaments are visually found to be directed toward the central part of the filamentary feature, and exhibit a temperature range of ~ 13 – 13.5 K in the *Herschel* temperature map.
- Five massive and dense clumps (“A”–“E”; $M_{\text{clump}} \sim 45$ – $300 M_\odot$; $n_{\text{H}_2} \sim 1.3$ – $5.5 \times 10^4 \text{ cm}^{-3}$) are identified toward the central part of the filamentary feature.
- The *Herschel* temperature map shows an extended temperature structure toward the central part of the filamentary feature. The infrared shell is spatially seen within this temperature structure at $T_d \sim 20$ – 26.5 K . Furthermore, an area with a substantial cold dust emission ($T_d \sim 13.5$ – 15 K) is also investigated inside this extended temperature structure.
- Based on the analysis of the *Spitzer* $8.0 \mu\text{m}$ image and the *Spitzer* ratio map of $4.5 \mu\text{m}/3.6 \mu\text{m}$ emission, the presence of PDRs in AFGL 5157 is traced. The observed extended temperature structure suggests the

distribution of the warm dust emission in the PDRs, revealing the signatures of the impact of massive stars in AFGL 5157.

- The *Spitzer* ratio map reveals the signatures of outflow activities toward the IRDCs seen in the *Spitzer* 8.0 μm image, where the *Herschel* column density map traces higher column density materials.

- Using the ^{12}CO and ^{13}CO line data, the molecular gas associated with AFGL 5157 is studied in a velocity range of $[-22, -15]$ km s^{-1} , and shows two velocity components around -20 and -17 km s^{-1} . Using the molecular line data, a bridge-like feature is investigated at the intermediate velocity range between these two velocity peaks.

- The central part of the *Herschel* filamentary feature is found at the overlapping zones of two filamentary molecular clouds (length ~ 12.5 pc) around -20 and -17 km s^{-1} , which are also connected in the velocity space. Considering the observed low ratio value (< 2.5) of $^{12}\text{CO}/^{13}\text{CO}$ at -18.5 km s^{-1} , self-absorption of ^{12}CO line is found toward the common areas of two clouds.

- Using the photometric analysis of point-like sources, embedded clusters of YSOs are found mainly toward the central part of the *Herschel* filamentary feature, and are distributed around the infrared shell. These embedded clusters are also located toward the spatial overlapping zones of the two filamentary molecular clouds (around -20 and -17 km s^{-1}). In the direction of the central part, the maximum value of the column density is found to be $\sim 3.7 \times 10^{23}$ cm^{-2} , favouring the appropriate condition for the birth of massive stars.

Overall, our findings suggest that the cloud-cloud collision operated in the past, which might have triggered the observed SF activities in AFGL 5157.

We thank the anonymous reviewer for several useful comments and suggestions, which greatly improved the scientific contents of the paper. The research work at Physical Research Laboratory is funded by the Department of Space, Government of India. This work is based on data obtained as part of the UKIRT Infrared Deep Sky Survey. This publication made use of data products from the Two Micron All Sky Survey (a joint project of the University of Massachusetts and the Infrared Processing and Analysis Center / California Institute of Technology, funded by NASA and NSF), archival data obtained with the *Spitzer* Space Telescope (operated by the Jet Propulsion Laboratory, California Institute of Technology under a contract with NASA). This paper makes use of data obtained as part of the INT Photometric $\text{H}\alpha$ Survey of the Northern Galactic Plane (IPHAS, www.iphas.org) carried out at the Isaac Newton Telescope (INT). The INT is operated on the island of La Palma by the Isaac Newton Group in the Spanish Observatorio del Roque de los Muchachos of the Instituto de Astrofísica de Canarias. The IPHAS data are processed by the Cambridge Astronomical Survey Unit, at the Institute of Astronomy in Cambridge. WISE is a joint project of the University of California and the JPL, Caltech, funded by the NASA. IRAF is distributed by the National Optical Astronomy Observatory, USA. The Canadian Galactic Plane Survey (CGPS) is a Canadian project with international part-

ners. The Dominion Radio Astrophysical Observatory is operated as a national facility by the National Research Council of Canada. The Five College Radio Astronomy Observatory CO Survey of the Outer Galaxy was supported by NSF grant AST 94-20159. The CGPS is supported by a grant from the Natural Sciences and Engineering Research Council of Canada.

REFERENCES

- Anathpindika, S. V. 2010, MNRAS, 405, 1431
 André, P., Men'shchikov, A., Bontemps, S., et al. 2010, A&A, 518, L102
 André, P., Di Francesco, J., Ward-Thompson, D., et al. 2014, in Protostars and Planets VI, ed. H. Beuther et al. (Tucson, AZ; Univ. Arizona Press), 27
 Balfour, S. K., Whitworth, A. P., & Hubber, D. A. 2017, MNRAS, 465, 3483
 Benjamin, R. A., Churchwell, E., Babler, B. L., et al. 2003, PASP, 115, 953
 Bisbas, T. G., Tanaka, K. E. I., Tan, J. C., Wu, B., & Nakamura, F. 2017, ApJ, 850, 23
 Bressert, E., Bastian, N., Gutermuth, R., et al. 2010, MNRAS, 409, 54
 Bressert, E., Ginsburg, A., Bally, J., et al. 2012, ApJ, 758, 28
 Brunt C., 2004, in Clemens D., Shah R., Brainerd T., eds, Proc. of ASP Conference 317. Milky Way Surveys: The Structure and Evolution of our Galaxy, p. 79
 Casertano, S., & Hut P. 1985, ApJ, 298, 80
 Chen, Y., Yao, Y., Yang, J., et al. 1999, AJ, 117, 446
 Chen, Y., Yao, Y., Yang, J., Zeng, Q., & Sato, S. 2003, A&A, 405, 655
 Churchwell, E., Povich, M. S., Allen, D., et al. 2006, ApJ, 649, 759
 Di Francesco, J., Johnstone, D., Kirk, H., MacKenzie, T., & Ledwosinska, E. 2008, ApJS, 175, 277
 Dewangan, L. K., Ojha, D. K., Anandarao, B. G., Ghosh, S. K., & Chakraborti, S. 2012, ApJ, 756, 151
 Dewangan, L. K., Luna, A., Ojha, D. K., et al. 2015, ApJ, 811, 79
 Dewangan, L. K., Ojha, D. K., Zinchenko, I., Janardhan, P., & Luna, A. 2017, ApJ, 834, 22
 Dewangan, L. K., Sano, H., Enokiya, R., et al. 2019a, ApJ, 878, 26
 Dewangan, L. K., Ojha, D. K., Baug, T., & Devaraj, R. 2019b, ApJ, 875, 138
 Drew, J. E., Greimel, R., Irwin, M. J., et al. 2005, MNRAS, 362, 753
 Duarte-Cabral, A., Dobbs, C. L., Peretto, N., Fuller, G. A. 2011, A&A, 528, 50
 Evans, N. J., II, Dunham, M. M., Jørgensen, J. K., et al. 2009, ApJS, 181, 321
 Flaherty, K. M., Pipher, J. L., Megeath, S. T., et al. 2007, ApJ, 663, 1069
 Fontani, F., Caselli, P., Zhang, Q., et al. 2012, 541, 32
 Fukui, Y., Ohama, A., Hanaoka, N., et al. 2014, ApJ, 780, 36
 Fukui, Y., Torii, K., Hattori, Y., et al. 2018, ApJ, 859, 166
 Galván-Madrid, R., Zhang, Q., Keto, E., et al. 2010, ApJ, 725, 17
 Gutermuth, R. A., Megeath, S. T., Myers, P. C., et al. 2009, ApJS, 184, 18
 Habe, A., & Ohta, K. 1992, PASJ, 44, 203
 Haworth, T. J., Tasker, E. J., Fukui, Y., et al. 2015a, MNRAS, 450, 10
 Haworth, T. J., Shima, K., Tasker, E. J., et al. 2015b, MNRAS, 454, 1634
 Henshaw, J. D., Caselli, P., Fontani, F., Jiménez-Serra, I., Tan, J. C., & Hernandez, A. K. 2013, MNRAS, 428, 3425
 Heyer, M. H., Carpenter, J. M., & Ladd, E. F. 1996, ApJ, 463, 630
 Heyer, M., Brunt, C., Snell, R., et al. 1998, ApJS, 115, 241
 Inoue, T., & Fukui, Y. 2013, ApJL, 774, 31
 Jiang, Z., Chen, Z., Wang, Y., et al. 2013, RAA, 13, 695
 Klein, R., Posselt, B., Schreyer, K., Forbrich, J., & Henning, T. 2005, ApJS, 161, 361
 Krumholz, M., R., & McKee, C., F. 2008, Nature, 451, 1082
 Lada, C. J., Muench, A. A., Luhman, K. L., et al. 2006, AJ, 131, 1574

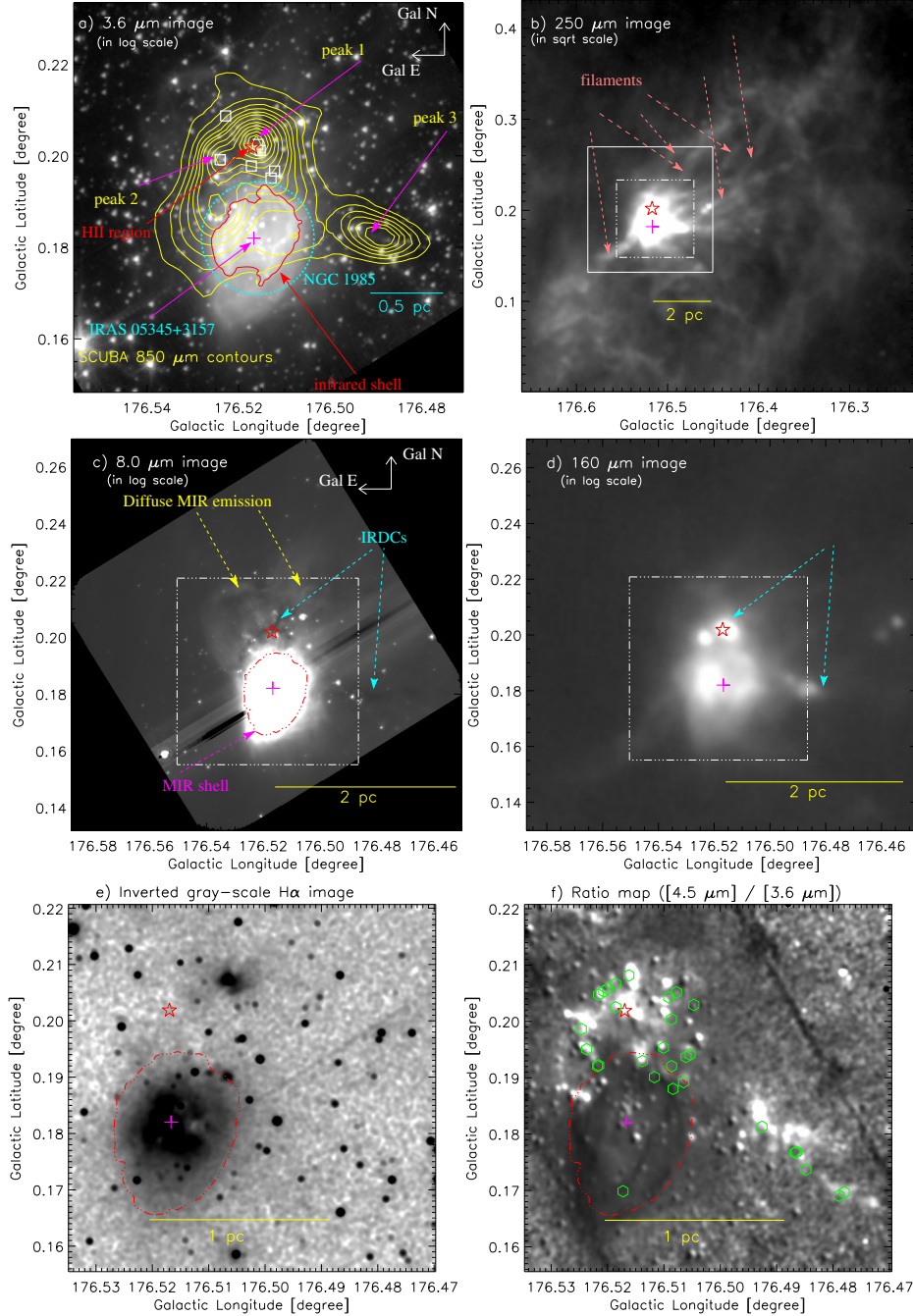
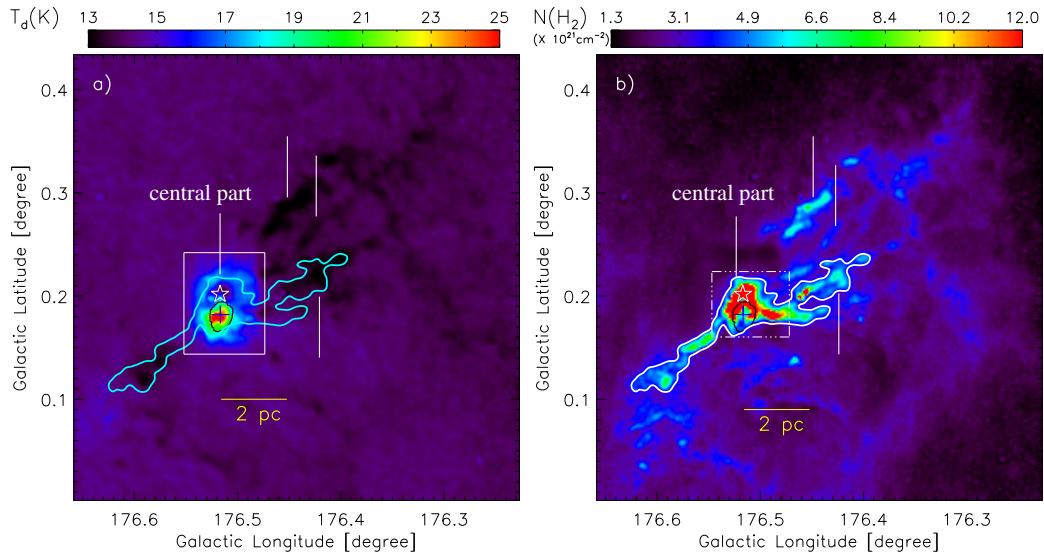


Figure 1. Infrared view of AFGL 5157 at different spatial scales. a) *Spitzer* 3.6 μm image (size $\sim 5'.1 \times 5'.1$ or $\sim 2.7 \text{ pc} \times 2.7 \text{ pc}$ (at a distance of 1.8 kpc)). The SCUBA 850 μm contours (in yellow; Di Francesco et al. 2008) are shown with the levels of $2.64 \text{ Jy/beam} \times (0.05, 0.1, 0.15, 0.2, 0.25, 0.3, 0.4, 0.5, 0.6, 0.7, 0.8, 0.9, \text{ and } 0.95)$. The positions of the identified CS cores (from Lee et al. 2011) are also marked in the figure (see white squares). Using the *Spitzer* 3.6 μm continuum emission contour (in red; level = 7.8 MJy/sr), an infrared shell-like feature is indicated in the figure. The area shown in this figure is marked by a broken box in Figure 1b. b) A large-scale view of AFGL 5157 at *Herschel* 250 μm (size $\sim 0'.43 (13.5 \text{ pc}) \times 0'.43 (13.5 \text{ pc})$; central coordinates: $l = 176'.445$; $b = 0'.215$). The solid box (in white) encompasses the area shown in Figure 1c. c) *Spitzer* image at 8.0 μm (see a solid box in Figure 1b). IRDCs, infrared shell, and diffused emissions are highlighted by arrows. The broken box (in white) encompasses the area shown in Figures 1e and 1f. d) *Herschel* image at 160 μm (see a solid box in Figure 1b). e) Inverted gray-scale IPHAS $\text{H}\alpha$ image (see a broken box in Figure 1d). f) *Spitzer* ratio map of 4.5 $\mu\text{m}/3.6 \mu\text{m}$ emission (see a broken box in Figure 1d). Hexagons (in green) show the locations of MHOs reported by Wolf-Chase et al. (2017) (see also Figure 6b in their paper). The $\text{H}\alpha$ image and the ratio map are smoothed using a Gaussian function with radius of four (see panels “e” and “f”). In each panel, a plus symbol shows the location of the IRAS 05343+3157 source. In the panels, a scale bar (at a distance of 1.8 kpc) is displayed, and a star symbol represents the location of an H II region (from Torrelles et al. 1992b). The infrared shell-like feature is highlighted by the *Spitzer* 8 μm contour (in red; level = 70 MJy/sr) in the panels “c”, “e”, and “f”.



Embedded Herschel Clumps

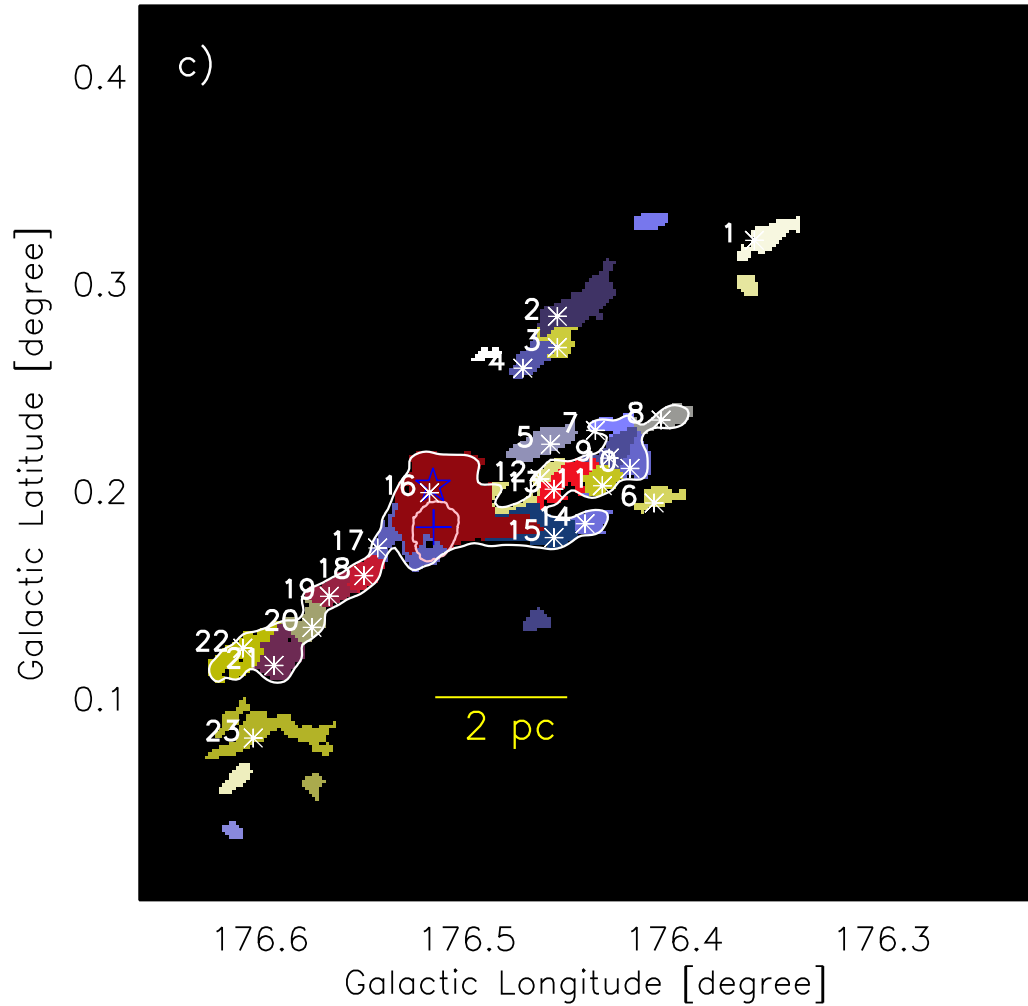


Figure 2. a) *Herschel* temperature map of the region around AFGL 5157. The solid box (in white) encompasses the area shown in Figures 3c and 3d. b) *Herschel* column density ($N(\text{H}_2)$) map. The broken box (in white) encompasses the area shown in Figures 3a and 3b. c) The identified clumps are marked by asterisks and the boundary of each *Herschel* clump is also displayed in the figure. The boundary of each *Herschel* clump is shown along with its corresponding clump ID (see also Table 2). In each panel, the filamentary feature is traced in the column density map at a contour level of $3.94 \times 10^{21} \text{cm}^{-2}$. In all the panels, other marked symbols and labels are similar to those shown in Figure 1.

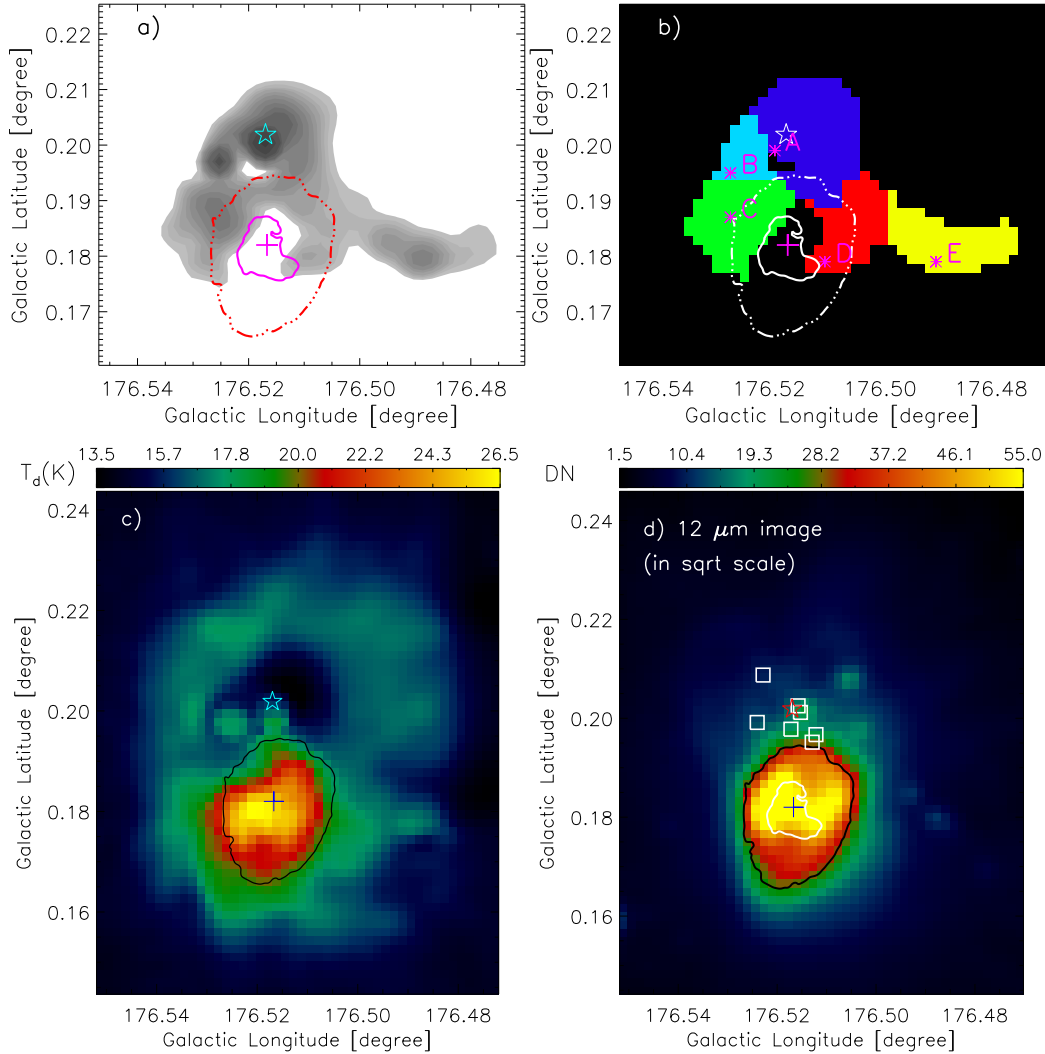


Figure 3. a) A zoomed-in view of the central part of the filamentary feature using the *Herschel* column density contour map. The $N(\text{H}_2)$ contours are shown with the levels of (9, 11, 13, 15, 19, 23, 30, 40, 50, 60, 90, 110, 180, and 300) $\times 10^{21} \text{ cm}^{-2}$. b) Five clumps are marked by asterisks, and are labeled as A, B, C, D, and E in the figure (see also Table 2). c) *Herschel* temperature map of an area highlighted by a solid box (in white) in Figure 2a. d) WISE image at $12 \mu\text{m}$ of an area highlighted by a solid box (in white) in Figure 2a. The positions of the identified CS cores (from Lee et al. 2011) are also marked in the WISE $12 \mu\text{m}$ image (see white squares). In the panels “a” and “b”, a solid contour shows the diffuse $\text{H}\alpha$ emission (see also Figures 1e and 1f). In all the panels, other marked symbols and labels are similar to those shown in Figure 1.

Lawrence, A., Warren, S. J., Almaini, O., et al. 2007, *MNRAS*, 379, 1599
 Lee, K. I., Looney, L. W., Klein, R., & Wong, S. 2011, *MNRAS*, 415, 2790
 Lucas, P. W., Hoare, M. G., Longmore, A., et al. 2008, *MNRAS*, 391, 1281
 Loren, R. B. 1976, *ApJ*, 209, 466
 Marsh, K. A., Whitworth, A. P., & Lomax, O. 2015, *MNRAS*, 454, 4282
 Marsh, K. A., Whitworth, A. P., Lomax, O., et al. 2017, *MNRAS*, 471, 2730
 Molinari, S., Swinyard, B., Bally, J., et al. 2010a, *A&A*, 518, L100
 Molinari, S., Swinyard, B., Bally, J., et al. 2010b, *PASP*, 122, 314
 Myers, P. C. 2009, *ApJ*, 700, 1609
 Nakamura, F., Miura, T., Kitamura, Y., et al. 2012, *ApJ*, 746, 25
 Nakamura, F., Sugitani, K., Tanaka, T., et al. 2014, *ApJL*, 791, L23
 Pastor, J., Estalella, R., Lopez, R., Anglada, G., & Planesas, P. 1991, *A&A*, 252, 320
 Reipurth, B. (ed.) 2008, *Handbook of Star Forming Regions*, Vol. I (San Francisco, CA: ASP)

Schneider, N., Csengeri, T., Hennemann, M., et al. 2012, *A&A*, 540, L11
 Skrutskie, M. F., Cutri, R. M., Stiening, R., et al. 2006, *AJ*, 131, 1163
 Snell, R. L., Huang, Y.-L., Dickman, R. L., & Claussen, M. J. 1988, *ApJ*, 325, 853
 Torrelles, J. M., Airoa, C., Miranda, L. F., et al. 1992a, *ApJ*, 384, 528
 Torrelles, J. M., Gomez, J. F., Anglada, G., et al. 1992b, *ApJ*, 392, 616
 Torii, K., Hattori, Y., Hasegawa, K., et al. 2017, *ApJ*, 835, 142
 Varricatt, W. P., Davis, C. J., Ramsay, S., & Todd, S. P. 2010, *MNRAS*, 404, 661
 Verdes-Montenegro, L., Torrelles, J. M., & Rodriguez, F., et al. 1989, *ApJ*, 346, 193
 Whitney, B., Benjamin, R., Meade, M., et al. 2011, *BAAS*, 43, 241.16
 Williams, J. P., de Geus, E. J., & Blitz, L. 1994, *ApJ*, 428, 693
 Wolf-Chase, G., Arvidsson, K., & Smutko, M. 2017, *ApJ*, 844, 38
 Wright, E. L., Eisenhardt, P. R. M., Mainzer, A. K., et al. 2010, *AJ*, 140, 1868
 Zhang, Q., Hunter, T. R., Brand, J., et al. 2005, *ApJ*, 625, 864

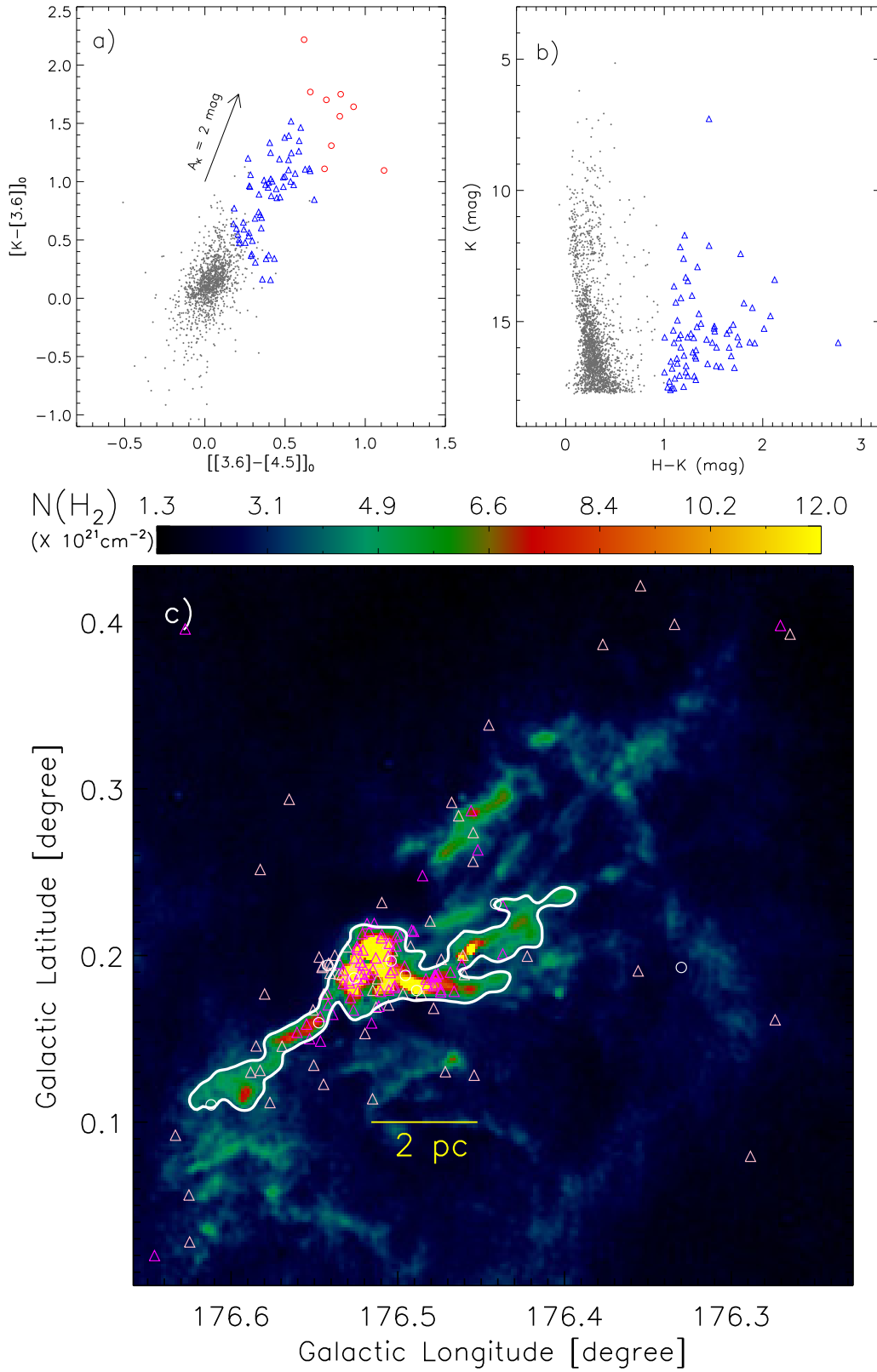


Figure 4. a) The panel displays the dereddened $[K-[3.6]]_0$ vs $[[3.6]-[4.5]]_0$ color-color plot of sources detected within our selected region (see Figure 1a). The extinction vector (from Flaherty et al. 2007) is shown in the figure. b) The panel displays the color-magnitude plot ($H-K/K$) of the sources. In the panels “a” and “b”, Class I and Class II YSOs are marked by red circles and open blue triangles, respectively. In the panels “a” and “b”, dot symbols (in gray color) refer stars with only photospheric emission. The positions of all the identified YSOs are marked in Figure 4c. c) Overlay of the selected YSOs on the *Herschel* column density map (see circles and triangles). The filamentary feature is also indicated by the column density contour with a level of $3.94 \times 10^{21} \text{ cm}^{-2}$ (see also Figure 2b).

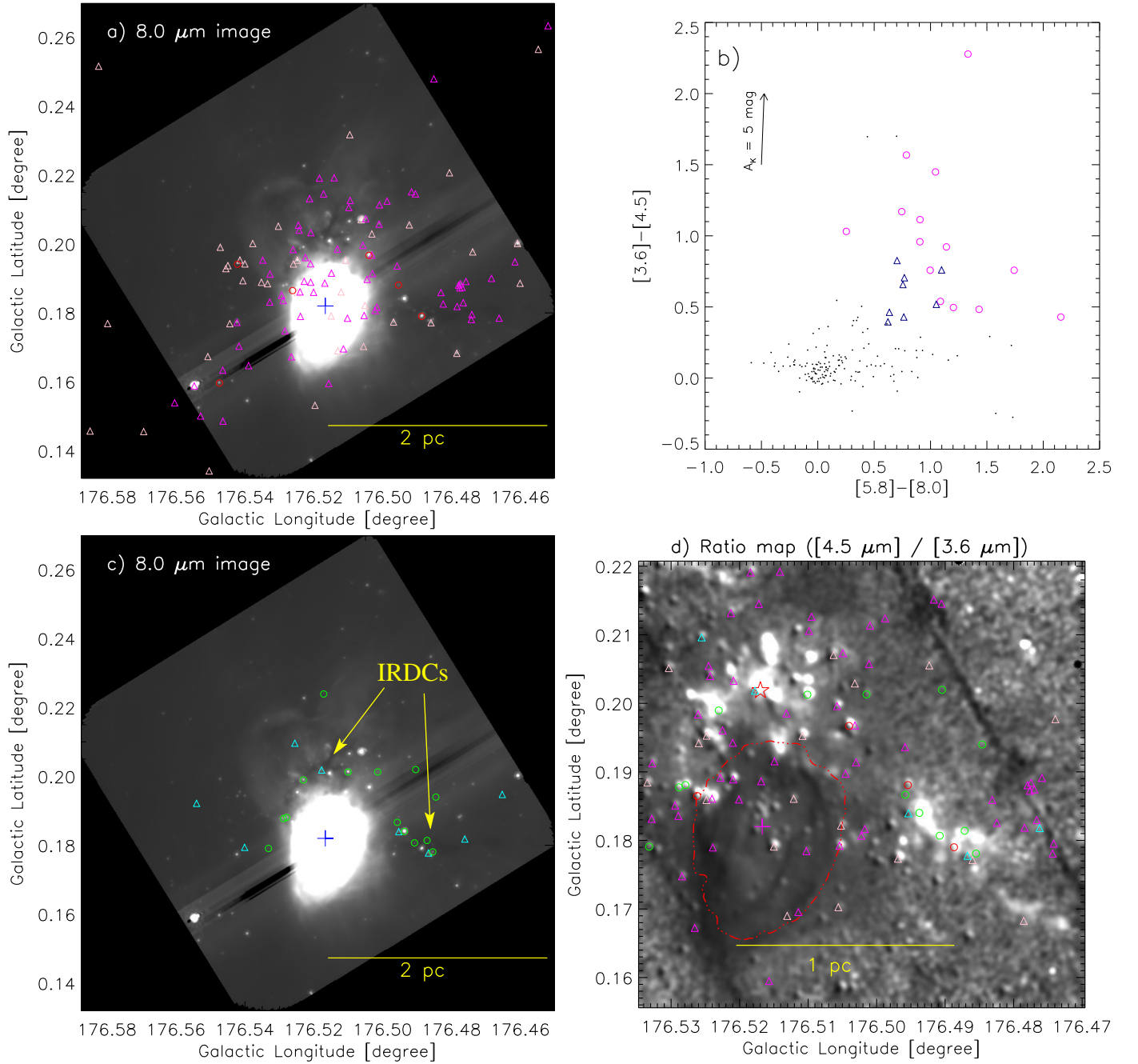


Figure 5. a) Overlay of the positions of the selected YSOs on the *Spitzer* 8.0 μm image (see also Figure 4c). b) Color-color plot ([3.6]–[4.5] vs. [5.8]–[8.0]) of sources detected in the *Spitzer* 3.6–8.0 μm images. An extinction vector (from Flaherty et al. 2007) is shown in the figure. Dot symbols (in gray color) show stars with only photospheric emission. Circles and triangles show Class I and Class II YSOs, respectively. c) Overlay of the positions of the additional YSOs on the *Spitzer* 8.0 μm image (from Figure 5b). d) Overlay of the positions of all the selected YSOs on the *Spitzer* ratio map of 4.5 μm /3.6 μm emission (see Figures 5a and 5c). The ratio map is the same as in Figure 1f.

Table 1
Multi-wavelength surveys used in this observational work.

Survey	Wavelength(s)	Resolution ($''$)	Reference
Extended Outer Galaxy Survey (E-OGS)	2.6–2.7 mm (CO(1-0))	~ 45 –46	Brunt (2004)
SCUBA Legacy Catalogues and continuum maps	850 μm	~ 19	Di Francesco et al. (2008)
<i>Herschel</i> Infrared Galactic Plane Survey (Hi-GAL)	70, 160, 250, 350, 500 μm	~ 5.8 , ~ 12 , ~ 18 , ~ 25 , ~ 37	Molinari et al. (2010a)
Wide Field Infrared Survey Explorer (WISE)	12 μm	~ 6	Wright et al. (2010)
Warm- <i>Spitzer</i> GLIMPSE360 Survey	3.6, 4.5 μm	~ 2 , ~ 2	Whitney et al. (2011); Benjamin et al. (2003)
UKIRT near-infrared Galactic Plane Survey (GPS)	1.25–2.2 μm	~ 0.8	Lawrence et al. (2007)
Two Micron All Sky Survey (2MASS)	1.25–2.2 μm	~ 2.5	Skrutskie et al. (2006)
INT Photometric H α Survey of the Northern Galactic Plane (IPHAS)	0.6563 μm	~ 1	Drew et al. (2005)

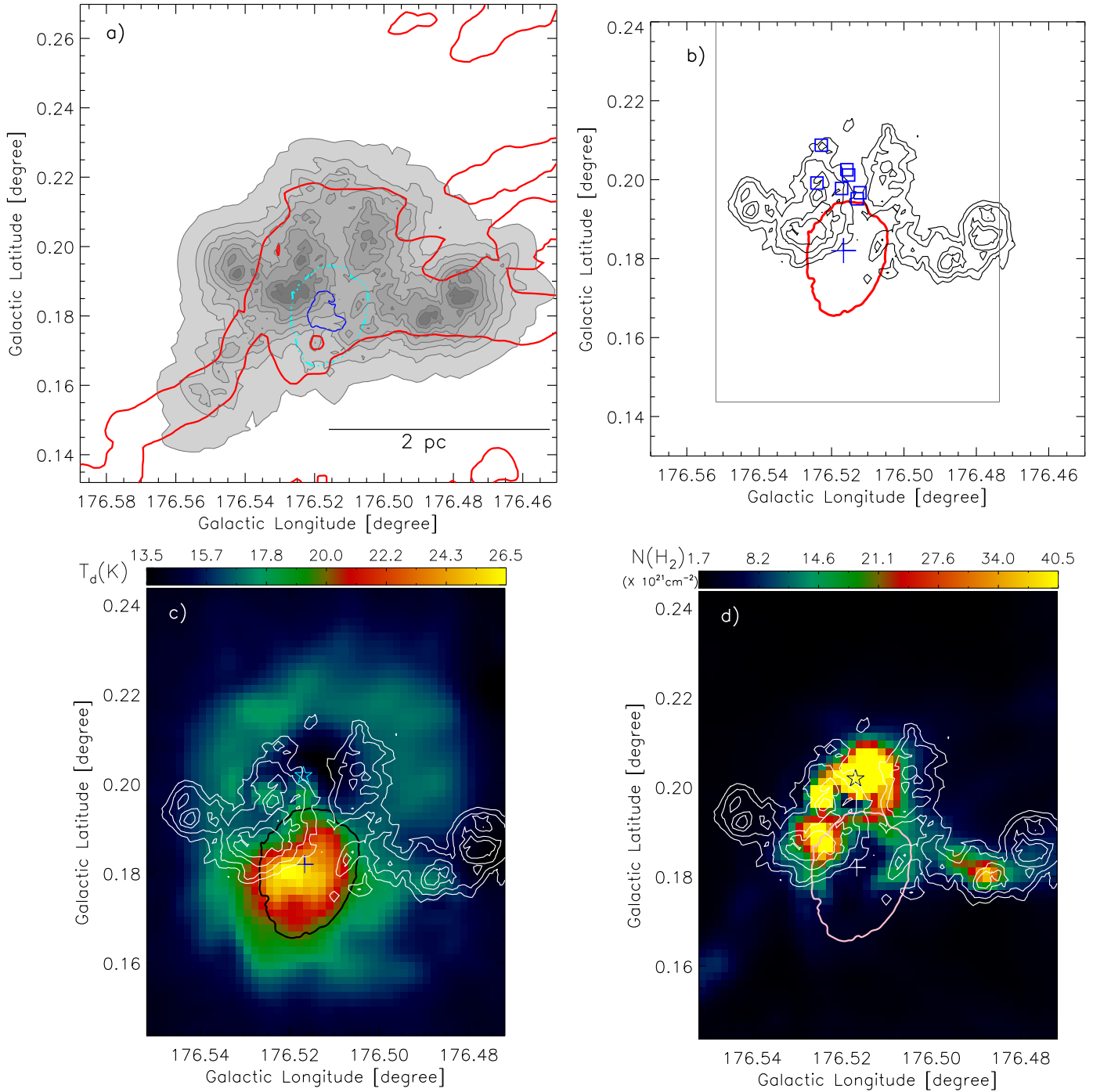


Figure 6. a) The panel shows the surface density contour map (in gray scale) of all the identified YSOs (see Figures 5a and 5c). The surface density contours are also shown with the levels of 5, 10, 15, 20, 30, 40, 60, and 85 YSOs/ pc^2 , from the outer to the inner side. The *Herschel* column density contours (in red), the *Spitzer* 8.0 μm emission contour (in cyan), and the $\text{H}\alpha$ emission contour (in blue) are also marked in the figure. b) Surface density contours of YSOs (in black) against the location of the infrared shell (see red contour). Blue squares represent the positions of the identified CS cores (from Lee et al. 2011). c) Overlay of the surface density contours (in white) on the *Herschel* temperature map. d) Overlay of the surface density contours (in white) on the *Herschel* column density map. In the last three panels, the surface density contours are shown with the levels of 30, 40, 60, and 85 YSOs/ pc^2 . In all the panels, the infrared shell is indicated by the *Spitzer* 8.0 μm emission contour as in Figure 1c.

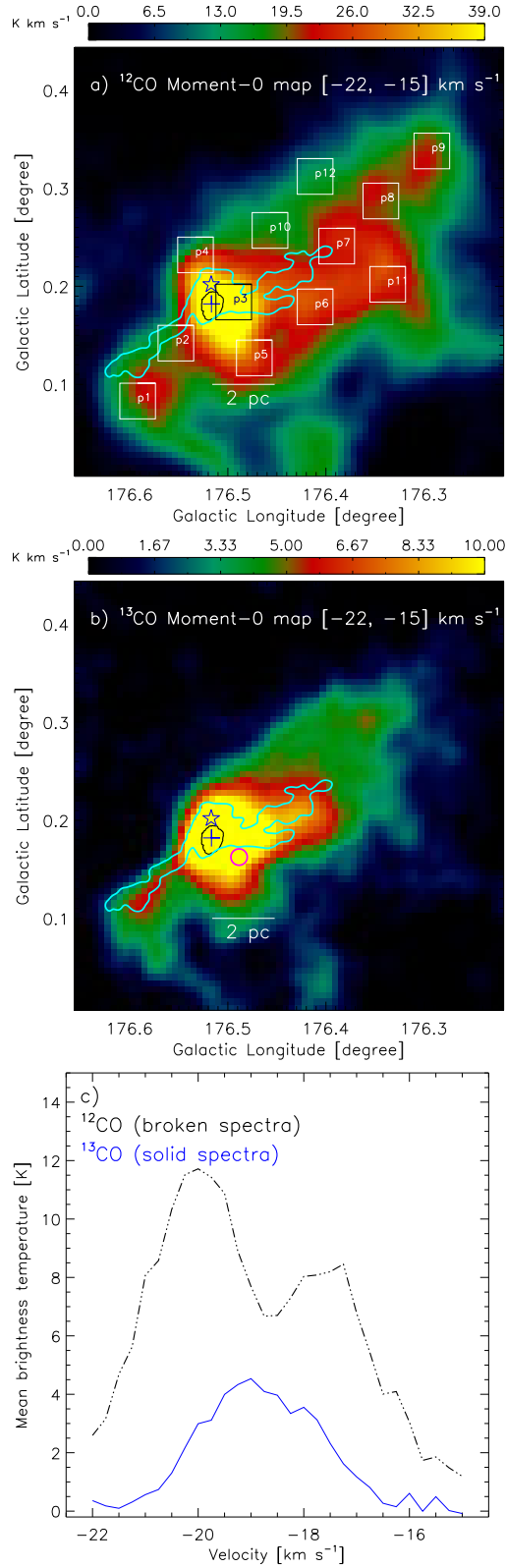


Figure 7. a) $^{12}\text{CO}(J=1-0)$ map of intensity (moment-0), integrated from -22 to -15 km s^{-1} . Twelve small regions (i.e. p1 to p12) are also indicated by boxes in the figure. b) $^{13}\text{CO}(J=1-0)$ map of intensity (moment-0), integrated from -22 to -15 km s^{-1} . In the panels “a” and “b”, the *Herschel* column density contour (in cyan) is also overlaid on the molecular map with a level of $3.94 \times 10^{21} \text{ cm}^{-2}$, indicating the location of the *Herschel* filamentary feature. c) The panel displays the ^{12}CO and ^{13}CO spectra. The profiles are obtained by averaging the area shown in Figure 7b (see a circle in Figure 7b). In the panels “a” and “b”, other marked symbols and labels are similar to those shown in Figure 1.

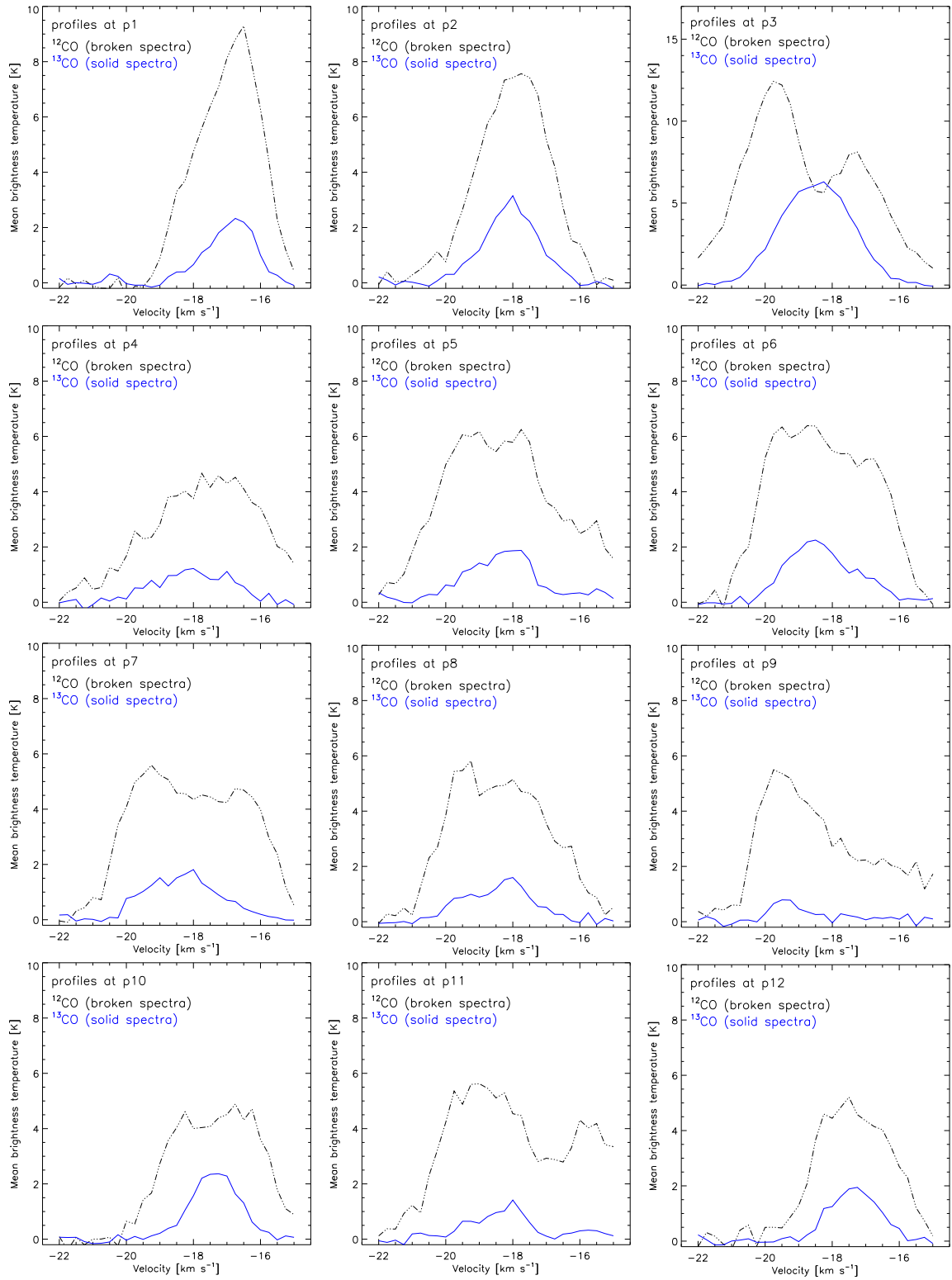


Figure 8. The ¹²CO and ¹³CO profiles in the direction of twelve small regions (i.e. p1 to p12; see corresponding boxes in Figure 7a).

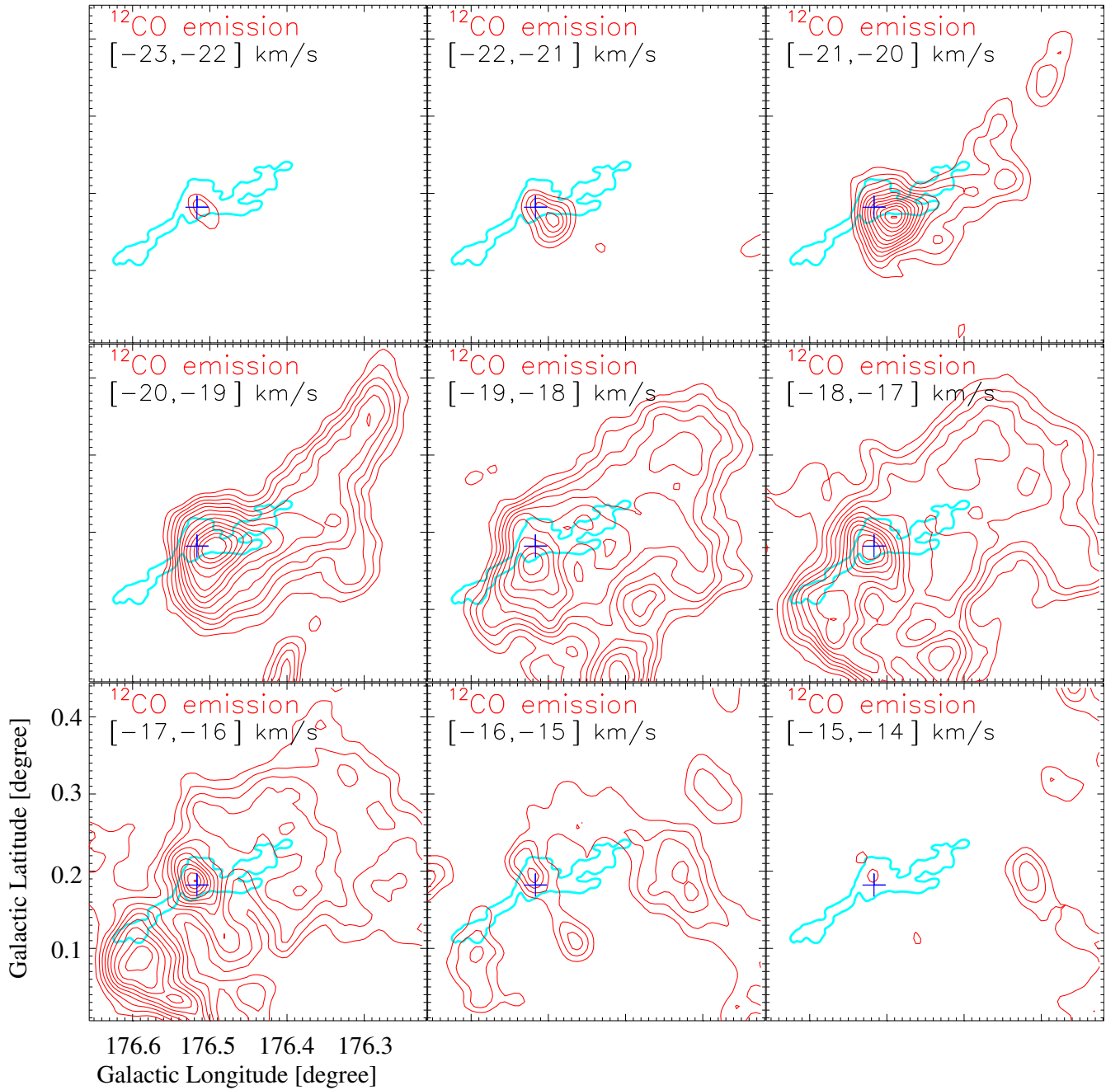


Figure 9. Velocity channel contours of ^{12}CO emission. The molecular emission is integrated over a velocity interval, which is marked in each panel (in km s^{-1}). The contour levels of ^{12}CO are presented with the levels of 2, 3, 4, 5, 6, 7, 8, 9, 10, 11, 12, 13, and 14 K km s^{-1} . In each panel, the filamentary feature is indicated by the column density contour with a level of $3.94 \times 10^{21} \text{ cm}^{-2}$ (see also Figure 2b). In all the panels, a plus symbol shows the location of the IRAS 05343+3157 source.

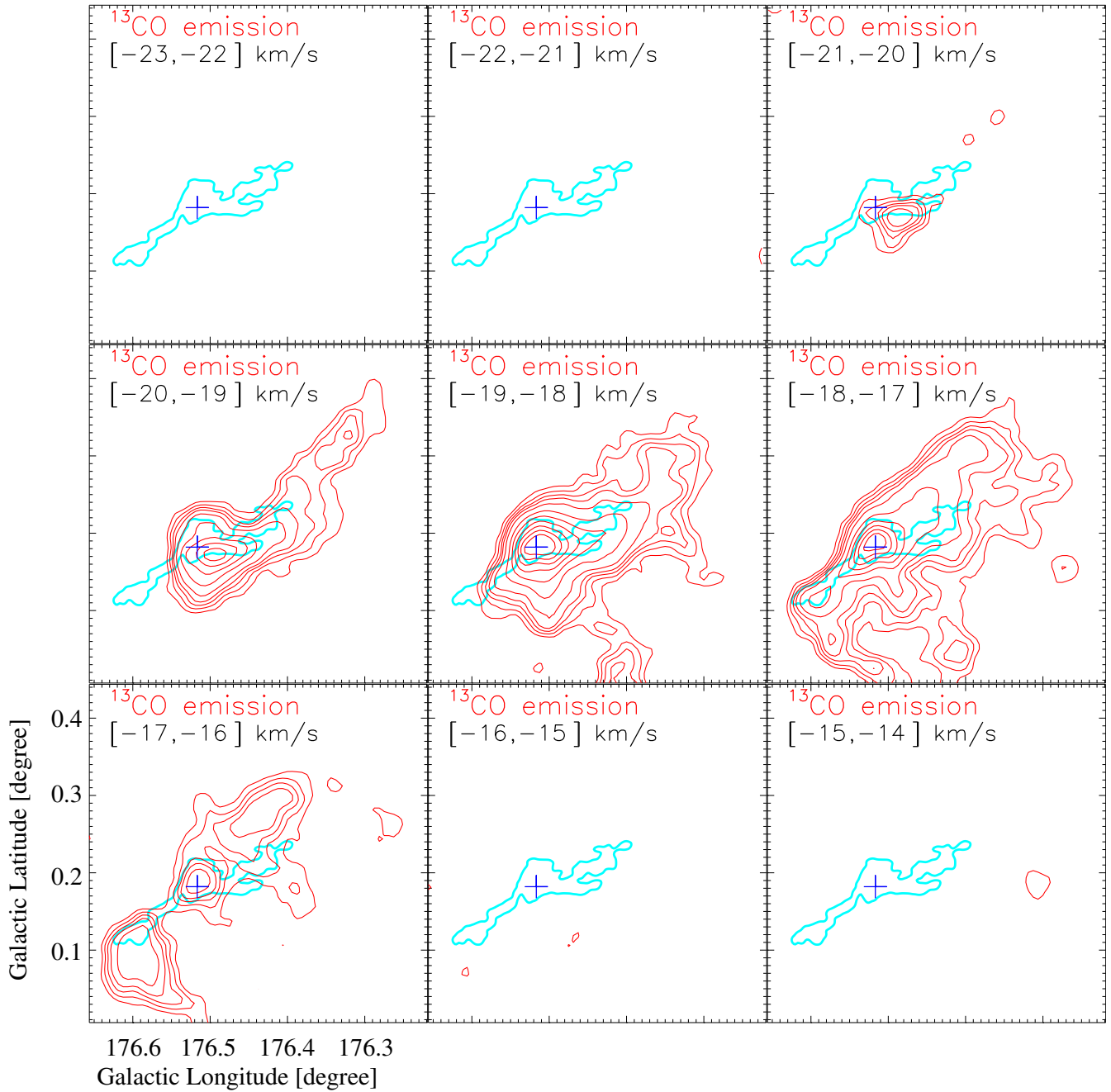


Figure 10. Velocity channel contours of ^{13}CO emission. The contour levels of ^{13}CO are presented with the levels of 0.6, 0.9, 1.2, 1.5, 2, 3, 4, 5, 6, 7, and 8 K km s^{-1} . In each panel, other marked symbols and the contour are similar to those shown in Figure 9.

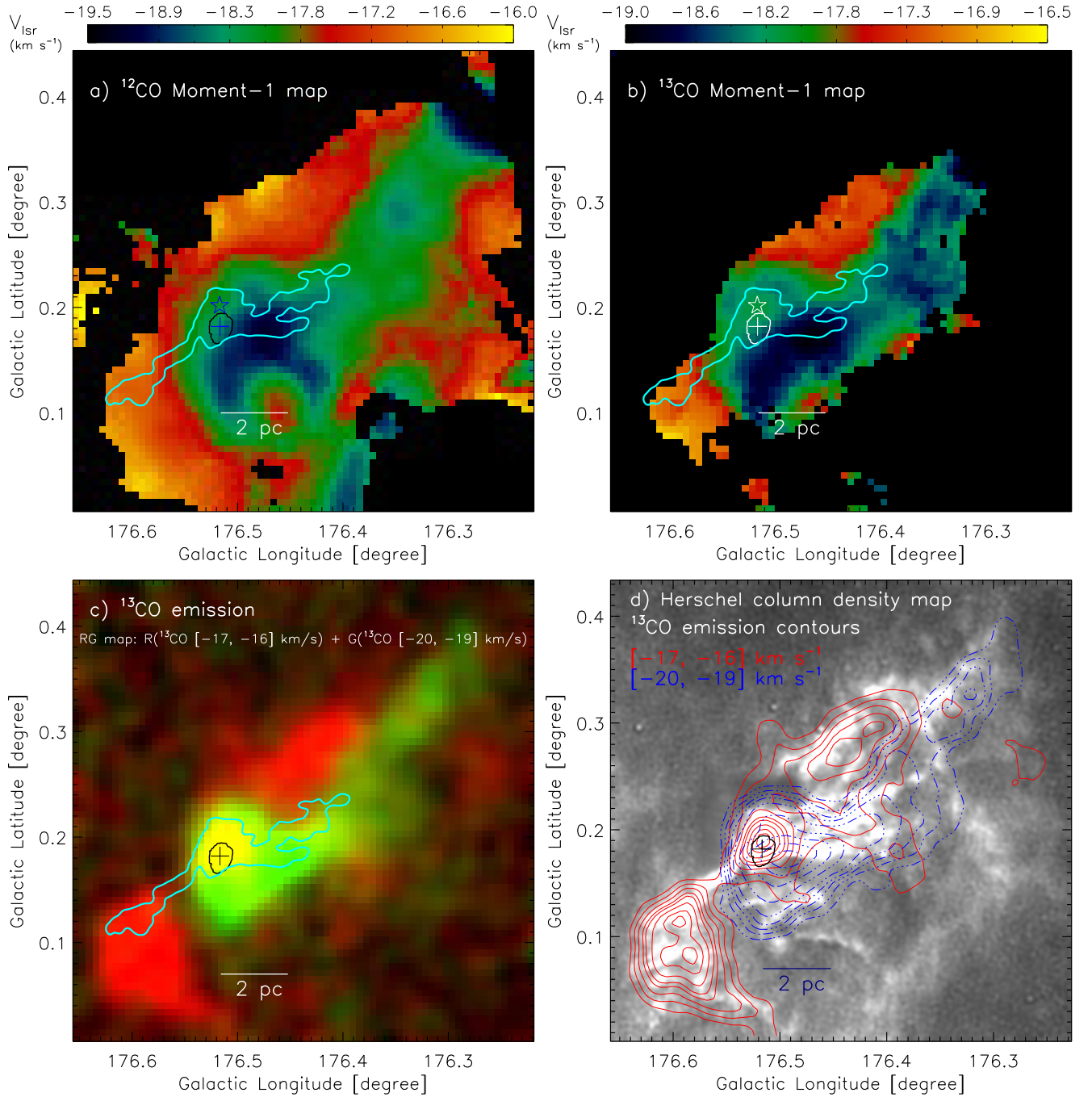


Figure 11. a) ^{12}CO first moment map. b) ^{13}CO first moment map. c) Two color-composite image produced using the ^{13}CO maps at $[-17, -16]$ and $[-20, -19]$ km s^{-1} in red and green, respectively. d) Overlay of the ^{13}CO emission contours (at $[-17, -16]$ and $[-20, -19]$ km s^{-1}) on the *Herschel* column density map. The velocity ranges are also given in the figure. The ^{13}CO emission contours at $[-17, -16]$ km s^{-1} (in red) are displayed with the levels of 0.6, 0.9, 1.2, 1.5, 1.7, 2, 2.3, and 2.5 K km s^{-1} , while the ^{13}CO emission contours at $[-20, -19]$ km s^{-1} (in blue) are 0.6, 0.9, 1.2, 1.5, 2, 3, 4, 5, 6, 7, and 8 K km s^{-1} . In each panel, other marked symbols and the contour are similar to those shown in Figure 2.

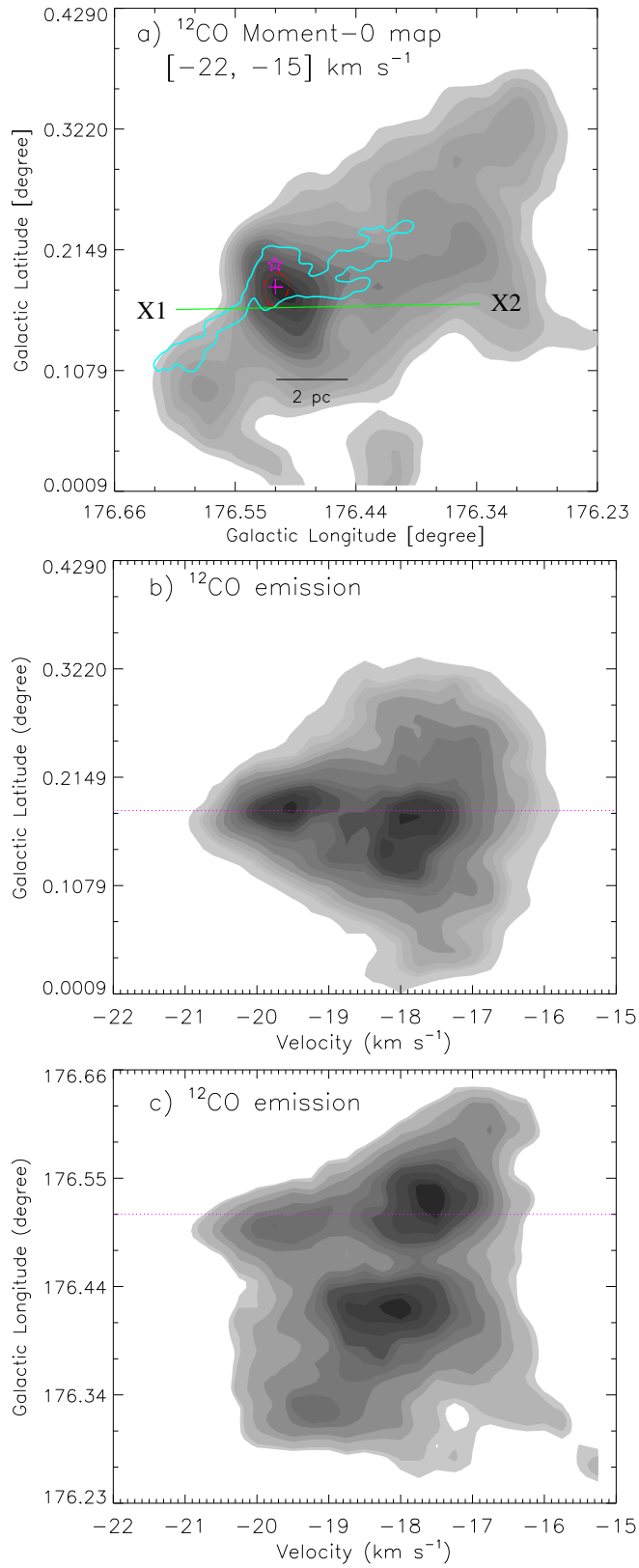


Figure 12. a) Contour map of the integrated ^{12}CO emission in a velocity range of -22 to -15 km s^{-1} . The ^{12}CO integrated intensity map is similar as in Figure 7a. Other marked symbols and contour are similar to those shown in Figure 2. A solid line (in green) shows the axis (i.e., X1–X2), where position-velocity maps are obtained (see Figures 13a and 13b). b) Latitude-velocity map of ^{12}CO . The molecular emission is integrated over the longitude from $176^\circ.23$ to $176^\circ.66$. c) Longitude-velocity map of ^{12}CO . The molecular emission is integrated over the latitude from $0^\circ.0009$ to $0^\circ.4290$. In the panels “b” and “c”, a dotted magenta line shows the position of the IRAS 05343+3157 source.

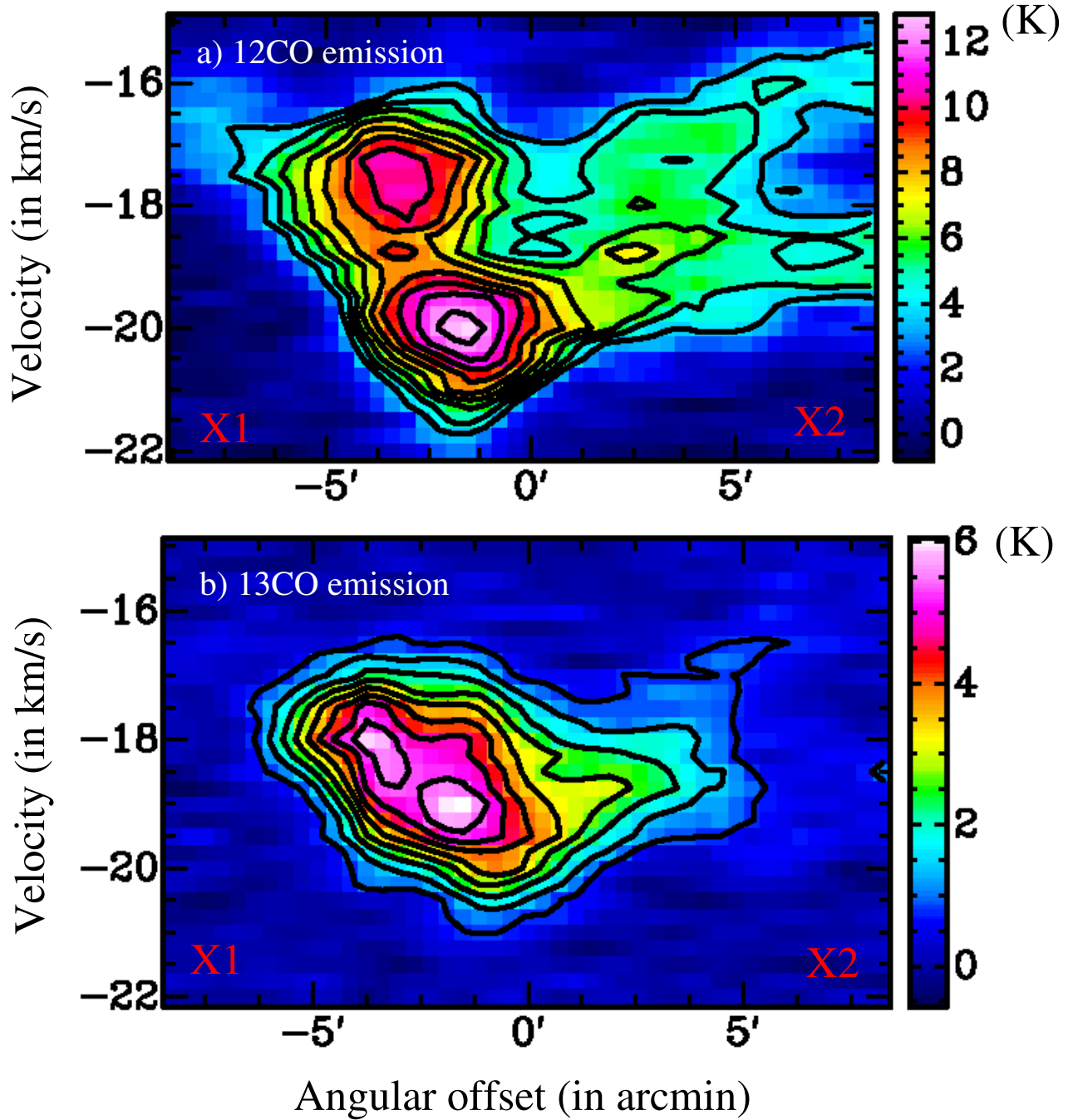


Figure 13. a) A position-velocity map of ^{12}CO along the axis (i.e., X1–X2) as highlighted in Figure 12a, depicting at least two cloud components (around -20 and -17 km s^{-1}) along the line-of-sight. b) A position-velocity map of ^{13}CO along the axis (i.e., X1–X2) as highlighted in Figure 12a. In both the panels, contours are also plotted to show different features.

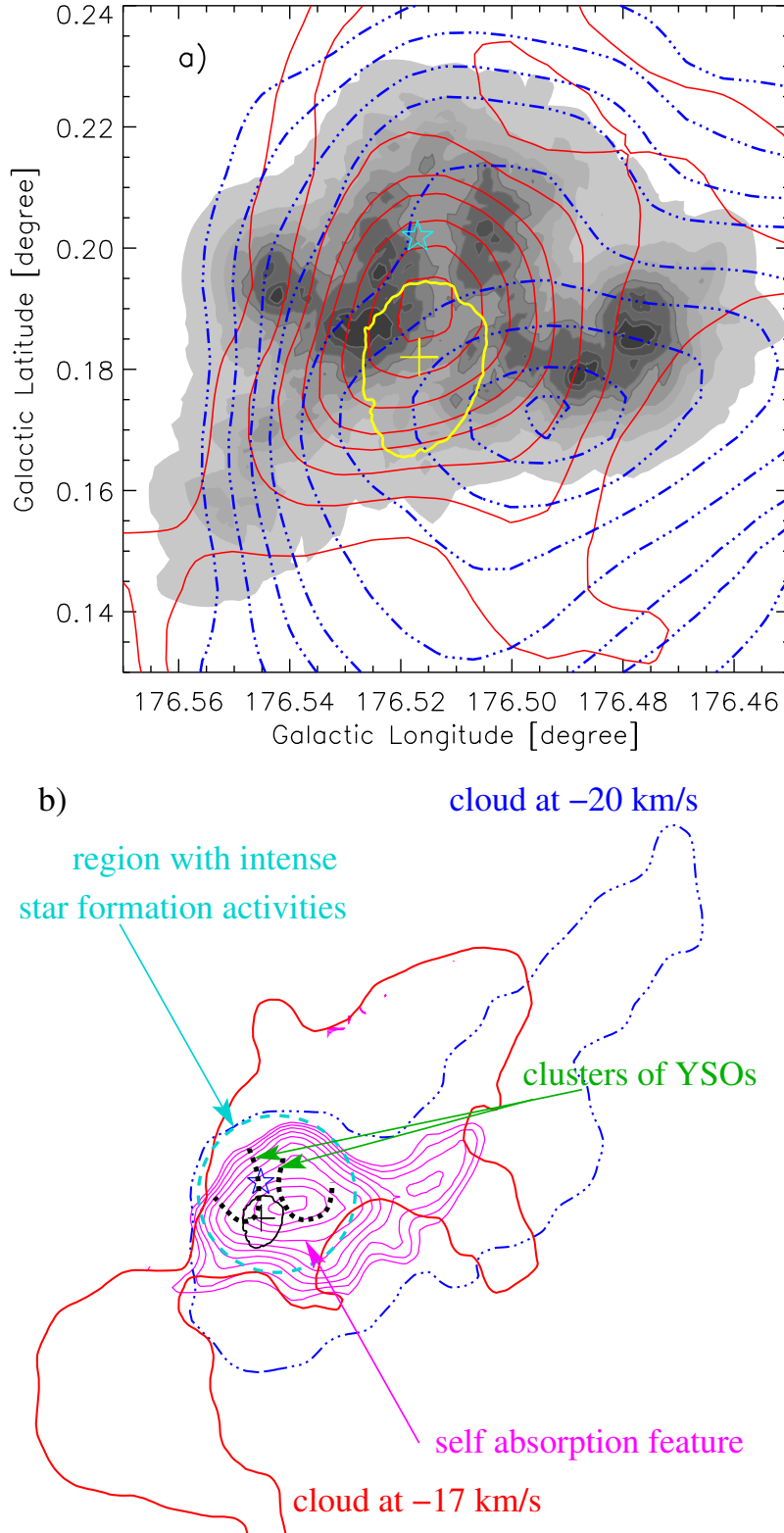


Figure 14. a) Overlay of the ^{13}CO emission contours (at $[-17, -16]$ and $[-20, -19]$ km s^{-1}) on the surface density contour map (see also Figure 6a). The area shown in this figure is same as in Figure 5c. The red contours show the ^{13}CO emission at $[-17, -16]$ km s^{-1} , while the blue contours represent the ^{13}CO emission at $[-20, -19]$ km s^{-1} (see also Figure 11d). Other marked symbols and the contour are similar to those shown in Figure 2. b) A schematic figure displays the spatial distribution of two clouds (around -20 and -17 km s^{-1}) at large-scale (see also Figure 11d). The region in the broken circle indicates the area associated with the intense SF activities (see also Figure 14a). Two arc-like curves represent the locations of the embedded clusters of YSOs (see also Figure 14a). The location of the ^{12}CO self-absorption feature is also marked by solid contours (in magenta; levels = $[0.8, 0.9, 1.0, 1.2, 1.4, 1.6, 1.8, 2.0, 2.2, 2.4]$), which is identified based on a low ratio value (< 2.5) of $^{12}\text{CO}/^{13}\text{CO}$ at -18.5 km s^{-1} .

Table 2

Properties of the selected *Herschel* clumps in AFGL 5157 (see Figures 2c and 3b). Clump IDs, positions, deconvolved effective radius (R_{clump}), clump mass (M_{clump}), and average volume density (n_{H_2}) are listed in the table. Twenty three clumps (i.e., 1–23) are labeled in Figure 2c, while five clumps (i.e., A–E) are labeled in Figure 3b.

ID	l (degree)	b (degree)	R_{clump} (pc)	M_{clump} (M_{\odot})	n_{H_2} (cm^{-3})
1	176.362	0.320	0.29	25	3540
2	176.457	0.284	0.43	65	2825
3	176.457	0.269	0.23	17	4830
4	176.474	0.259	0.28	27	4250
5	176.460	0.222	0.33	35	3365
6	176.410	0.194	0.23	16	4545
7	176.439	0.229	0.21	14	5225
8	176.407	0.234	0.25	20	4425
9	176.432	0.215	0.28	28	4410
10	176.422	0.210	0.26	23	4520
11	176.435	0.202	0.25	20	4425
12	176.465	0.205	0.26	20	3930
13	176.459	0.200	0.32	48	5065
14	176.444	0.184	0.23	17	4830
15	176.459	0.177	0.35	48	3870
16	176.519	0.199	0.80	724	4885
17	176.544	0.172	0.34	38	3340
18	176.550	0.159	0.26	28	5505
19	176.567	0.149	0.27	30	5270
20	176.575	0.134	0.28	25	3935
21	176.594	0.115	0.35	45	3625
22	176.609	0.124	0.37	43	2935
23	176.604	0.080	0.46	64	2270
A	176.519	0.199	0.32	300	31650
B	176.527	0.195	0.16	65	54860
C	176.527	0.187	0.27	110	19320
D	176.510	0.179	0.23	45	12785
E	176.490	0.179	0.25	65	14380

Table 3
Near-infrared and *Spitzer* IRAC/GLIMPSE photometric magnitudes of selected YSOs (see Figures 4c and 5c).

ID	<i>l</i>	<i>b</i>	J (mag)	H (mag)	K (mag)	3.6 μ m (mag)	4.5 μ m (mag)	5.8 μ m (mag)	8.0 μ m (mag)	Class
1	176.612	0.110	—	15.75	14.37	12.72	11.85	—	—	I
2	176.330	0.193	15.62	14.65	13.96	13.14	12.48	—	—	I
3	176.441	0.231	16.00	14.56	13.53	12.33	11.57	—	—	I
4	176.489	0.179	—	15.92	13.85	12.46	11.26	—	—	I
5	176.504	0.197	—	13.46	12.74	11.52	10.71	—	—	I
6	176.526	0.186	15.26	13.69	12.75	11.03	10.38	—	—	I
7	176.495	0.188	17.39	15.77	15.08	13.68	13.00	—	—	I
8	176.547	0.160	15.11	14.03	13.53	12.28	11.57	—	—	I
9	176.542	0.194	—	15.63	14.86	12.77	12.19	—	—	I
10	176.625	0.056	16.97	15.69	14.94	13.64	13.22	—	—	II
11	176.625	0.028	14.68	13.69	13.25	12.52	12.06	—	—	II
12	176.633	0.092	15.10	14.31	13.81	13.15	12.85	—	—	II
13	176.354	0.422	15.27	14.69	14.68	14.49	14.35	—	—	II
14	176.377	0.387	15.17	14.69	14.71	14.51	14.38	—	—	II
15	176.334	0.399	15.67	14.82	14.41	14.43	14.07	—	—	II
16	176.356	0.191	15.31	14.79	14.75	14.39	14.26	—	—	II
17	176.565	0.294	13.92	13.08	12.49	11.55	11.16	—	—	II
18	176.445	0.338	16.51	15.59	14.99	14.56	14.26	—	—	II
19	176.460	0.189	15.83	14.64	14.14	13.28	13.07	—	—	II
20	176.474	0.198	14.97	14.03	13.47	12.59	12.26	—	—	II
21	176.461	0.200	13.51	12.25	11.33	10.20	9.69	—	—	II
22	176.510	0.232	15.27	14.44	14.16	13.81	13.59	—	—	II
23	176.455	0.274	12.75	11.81	11.21	10.18	9.89	—	—	II
24	176.455	0.256	14.44	13.39	12.96	12.45	12.19	—	—	II
25	176.481	0.221	—	16.12	15.26	13.98	13.63	—	—	II
26	176.468	0.292	15.47	14.94	14.69	14.65	14.30	—	—	II
27	176.464	0.284	—	14.86	13.69	12.44	11.78	—	—	II
28	176.422	0.200	17.24	15.87	15.29	14.31	13.95	—	—	II
29	176.454	0.128	10.88	10.52	10.25	9.87	9.58	—	—	II
30	176.583	0.252	15.83	14.83	14.51	13.97	13.68	—	—	II
31	176.486	0.177	15.26	14.31	13.66	12.78	12.20	—	—	II
32	176.479	0.168	15.26	13.95	13.10	11.57	11.04	—	—	II
33	176.520	0.153	16.31	15.32	14.77	13.93	13.42	—	—	II
34	176.492	0.206	16.38	14.66	13.75	12.58	12.13	—	—	II
35	176.503	0.203	15.88	14.90	14.48	14.18	13.91	—	—	II
36	176.506	0.207	11.89	11.01	10.36	9.38	8.90	—	—	II
37	176.526	0.194	16.05	14.92	14.23	13.26	12.78	—	—	II
38	176.525	0.186	15.80	13.82	12.64	11.50	11.05	—	—	II
39	176.525	0.195	15.86	13.60	12.21	10.89	10.24	—	—	II
40	176.511	0.195	—	14.99	13.37	11.44	10.77	—	—	II
41	176.512	0.186	15.97	14.48	13.45	12.02	11.41	—	—	II
42	176.513	0.169	—	15.89	15.37	14.40	14.11	—	—	II
43	176.515	0.179	—	11.04	10.24	8.86	8.36	—	—	II
44	176.497	0.177	15.68	14.13	13.27	12.02	11.47	—	—	II
45	176.506	0.170	16.08	14.99	14.72	14.19	13.99	—	—	II
46	176.505	0.182	16.92	15.37	14.48	13.20	12.71	—	—	II
47	176.545	0.123	15.46	14.47	14.34	13.87	13.74	—	—	II
48	176.550	0.134	—	16.07	15.34	14.70	14.07	—	—	II
49	176.569	0.146	16.43	15.94	15.27	14.40	13.80	—	—	II
50	176.585	0.146	14.72	13.79	13.50	13.02	12.81	—	—	II
51	176.577	0.112	15.08	14.44	14.19	13.74	13.56	—	—	II
52	176.588	0.130	14.85	13.93	13.53	12.63	12.19	—	—	II
53	176.583	0.131	15.80	14.74	14.29	13.85	13.57	—	—	II
54	176.551	0.167	17.30	16.08	15.44	14.36	13.83	—	—	II
55	176.580	0.177	16.36	15.54	15.22	14.80	14.56	—	—	II
56	176.533	0.188	—	16.32	15.14	13.99	13.45	—	—	II
57	176.538	0.200	16.80	15.81	15.13	14.14	13.72	—	—	II
58	176.530	0.205	16.76	15.46	14.64	14.16	13.74	—	—	II
59	176.547	0.199	15.13	13.99	13.45	12.20	11.82	—	—	II
60	176.535	0.189	16.94	15.66	14.86	14.41	14.00	—	—	II
61	176.544	0.177	16.76	15.85	15.48	14.39	13.89	—	—	II
62	176.541	0.195	—	14.36	13.86	13.11	12.73	—	—	II
63	176.545	0.194	16.41	15.61	15.19	14.46	14.07	—	—	II
64	176.541	0.189	17.04	16.01	15.09	14.04	13.52	—	—	II
65	176.540	0.194	15.09	13.97	13.38	12.44	12.07	—	—	II
66	176.546	0.193	16.80	15.77	15.34	14.77	14.45	—	—	II
67	176.472	0.130	14.99	13.82	13.00	12.08	11.61	—	—	II
68	176.515	0.114	17.05	15.98	15.60	14.47	14.23	—	—	II
69	176.265	0.393	13.40	12.71	12.08	11.15	10.76	—	—	II
70	176.289	0.079	14.26	13.68	13.62	13.82	13.57	—	—	II
71	176.274	0.161	15.73	15.14	14.89	14.78	14.52	—	—	II
72	176.487	0.181	—	—	—	15.43	14.40	13.44	13.19	II
73	176.485	0.178	—	—	—	13.61	12.69	11.71	10.57	II
74	176.491	0.181	—	—	—	16.87	14.59	13.65	12.31	II
75	176.523	0.199	—	—	—	12.87	11.70	10.95	10.21	II
76	176.494	0.184	—	—	—	11.51	9.95	9.12	8.34	II
77	176.528	0.188	—	—	—	13.14	12.18	11.38	10.47	II
78	176.529	0.188	—	—	—	13.46	12.34	11.28	10.37	II
79	176.533	0.179	—	—	—	15.40	14.64	13.55	12.56	II
80	176.485	0.194	—	—	—	15.99	15.23	14.76	13.01	II
81	176.517	0.224	—	—	—	14.73	14.19	13.38	12.30	II
82	176.501	0.201	—	—	—	14.40	13.92	13.40	11.97	II
83	176.510	0.201	—	—	—	12.62	11.17	10.52	9.47	II

Table 4
Continuation of Table 3

ID	l	b	J (mag)	H (mag)	K (mag)	3.6 μm (mag)	4.5 μm (mag)	5.8 μm (mag)	8.0 μm (mag)	Class
84	176.490	0.202	—	—	—	15.15	14.72	14.49	12.34	I
85	176.496	0.187	—	—	—	15.78	15.29	14.64	13.44	I
86	176.465	0.195	—	—	—	15.63	15.17	14.66	14.03	II
87	176.487	0.178	—	—	—	12.57	11.86	11.38	10.62	II
88	176.476	0.182	—	—	—	14.35	13.69	13.02	12.27	II
89	176.518	0.202	—	—	—	13.10	12.28	11.77	11.07	II
90	176.495	0.184	—	—	—	12.64	12.24	11.82	11.20	II
91	176.526	0.210	—	—	—	14.64	14.12	13.80	12.75	II
92	176.540	0.179	—	—	—	15.47	14.71	14.30	13.20	II
93	176.554	0.192	—	—	—	14.60	14.17	13.95	13.19	II
94	176.437	0.230	18.64	16.73	15.46	—	—	—	—	II
95	176.462	0.195	17.08	15.27	14.10	—	—	—	—	II
96	176.456	0.287	19.63	17.86	16.78	—	—	—	—	II
97	176.542	0.177	16.21	14.25	12.92	—	—	—	—	II
98	176.546	0.163	20.17	17.29	15.80	—	—	—	—	II
99	176.546	0.149	19.18	17.49	16.29	—	—	—	—	II
100	176.542	0.170	—	18.47	16.76	—	—	—	—	II
101	176.437	0.201	19.56	17.59	16.52	—	—	—	—	II
102	176.501	0.211	19.83	16.81	15.11	—	—	—	—	II
103	176.501	0.206	17.25	14.19	12.42	—	—	—	—	II
104	176.505	0.207	18.28	16.11	14.30	—	—	—	—	II
105	176.503	0.197	18.28	16.91	15.81	—	—	—	—	II
106	176.503	0.191	20.22	17.63	16.32	—	—	—	—	II
107	176.505	0.190	20.25	17.51	15.98	—	—	—	—	II
108	176.502	0.182	18.54	16.42	15.33	—	—	—	—	II
109	176.502	0.181	19.15	17.41	16.09	—	—	—	—	II
110	176.505	0.179	19.73	16.86	14.79	—	—	—	—	II
111	176.506	0.200	—	17.28	15.27	—	—	—	—	II
112	176.521	0.213	19.82	16.88	15.37	—	—	—	—	II
113	176.524	0.204	18.51	16.05	14.70	—	—	—	—	II
114	176.523	0.189	19.43	16.37	14.47	—	—	—	—	II
115	176.521	0.189	14.54	12.92	11.71	—	—	—	—	II
116	176.524	0.186	18.43	15.53	13.40	—	—	—	—	II
117	176.527	0.167	18.70	16.67	15.50	—	—	—	—	II
118	176.525	0.205	—	18.27	17.17	—	—	—	—	II
119	176.521	0.194	—	18.29	16.72	—	—	—	—	II
120	176.522	0.196	—	17.65	15.99	—	—	—	—	II
121	176.526	0.198	—	18.57	15.81	—	—	—	—	II
122	176.485	0.248	18.45	16.44	15.07	—	—	—	—	II
123	176.482	0.183	20.41	18.21	17.05	—	—	—	—	II
124	176.483	0.186	—	18.54	17.22	—	—	—	—	II
125	176.533	0.191	19.46	17.91	16.69	—	—	—	—	II
126	176.529	0.185	19.44	16.77	15.26	—	—	—	—	II
127	176.529	0.184	18.97	16.92	15.62	—	—	—	—	II
128	176.533	0.183	—	17.63	15.87	—	—	—	—	II
129	176.528	0.175	—	17.99	16.31	—	—	—	—	II
130	176.535	0.195	18.35	16.61	15.60	—	—	—	—	II
131	176.539	0.165	18.15	16.09	14.95	—	—	—	—	II
132	176.476	0.189	19.44	17.15	15.98	—	—	—	—	II
133	176.477	0.187	19.59	17.45	16.16	—	—	—	—	II
134	176.477	0.188	15.11	13.32	12.16	—	—	—	—	II
135	176.478	0.187	16.47	14.75	13.65	—	—	—	—	II
136	176.478	0.188	15.87	13.56	12.11	—	—	—	—	II
137	176.474	0.178	18.64	16.53	15.20	—	—	—	—	II
138	176.478	0.182	19.99	16.99	15.32	—	—	—	—	II
139	176.474	0.180	—	17.74	15.82	—	—	—	—	II
140	176.477	0.183	—	18.22	16.69	—	—	—	—	II
141	176.468	0.190	19.22	17.53	16.40	—	—	—	—	II
142	176.466	0.178	—	18.33	17.28	—	—	—	—	II
143	176.646	0.020	18.52	16.69	15.18	—	—	—	—	II
144	176.514	0.219	19.28	18.64	17.54	—	—	—	—	II
145	176.518	0.219	18.95	16.83	15.59	—	—	—	—	II
146	176.517	0.215	19.34	17.94	16.93	—	—	—	—	II
147	176.521	0.203	19.31	17.11	15.68	—	—	—	—	II
148	176.515	0.192	16.50	14.53	13.31	—	—	—	—	II
149	176.517	0.189	17.09	15.39	14.27	—	—	—	—	II
150	176.516	0.159	19.53	18.54	17.50	—	—	—	—	II
151	176.271	0.398	19.96	18.61	17.54	—	—	—	—	II
152	176.452	0.263	19.86	18.31	17.07	—	—	—	—	II
153	176.553	0.150	19.07	17.72	16.59	—	—	—	—	II
154	176.510	0.213	20.36	18.15	16.93	—	—	—	—	II
155	176.510	0.211	19.90	17.09	15.46	—	—	—	—	II
156	176.513	0.199	19.45	18.67	17.60	—	—	—	—	II
157	176.510	0.178	17.55	15.29	14.01	—	—	—	—	II
158	176.511	0.170	19.93	18.38	17.08	—	—	—	—	II
159	176.491	0.215	19.77	17.72	16.40	—	—	—	—	II
160	176.492	0.215	18.87	16.78	15.63	—	—	—	—	II
161	176.560	0.154	19.77	17.33	15.59	—	—	—	—	II
162	176.628	0.396	20.06	18.68	17.48	—	—	—	—	II
163	176.499	0.212	20.34	18.05	16.61	—	—	—	—	II
164	176.496	0.194	—	17.65	15.79	—	—	—	—	II
165	176.520	0.186	14.97	14.69	13.45	—	—	—	—	II
166	176.524	0.179	15.76	13.80	12.60	—	—	—	—	II
167	176.555	0.159	11.55	8.73	7.27	—	—	—	—	II